CrossMark

J. Fluid Mech. (2017), *vol.* 826, *pp.* 553–582. © Cambridge University Press 2017
doi:10.1017/jfm.2017.426

Natural convection and thermal drift

Arman Abtahi[1,†] **and J. M. Floryan**[1]

[1]Department of Mechanical and Materials Engineering, University of Western Ontario, London, Ontario, N6A 5B9, Canada

(Received 24 January 2017; revised 30 April 2017; accepted 12 June 2017; first published online 8 August 2017)

An analysis of natural convection in a horizontal, geometrically non-uniform slot exposed to spatially non-uniform heating has been carried out. The upper plate is smooth and isothermal, and the lower plate has sinusoidal corrugations with a sinusoidal temperature distribution. The distributions of the non-uniformities are characterized in terms of the wavenumber α and their relative position is expressed in terms of the phase difference Ω_{TL}. The analysis is limited to heating conditions which do not give rise to secondary motions in the absence of the non-uniformities. The heating creates horizontal temperature gradients which lead to the formation of vertical and horizontal pressure gradients which drive the motion regardless of the intensity of the heating. When the hot spots (points of maximum temperature) overlap either with the corrugation tips or with the corrugation bottoms, convection assumes the form of pairs of counter-rotating rolls whose size is dictated by the heating/corrugation wavelengths. The formation of a net horizontal flow, referred to as thermal drift, is observed for all other relative positions of the hot spots and corrugation tips. Both periodic heating as well as periodic corrugations are required for the formation of this drift, which can be directed in the positive as well as in the negative horizontal directions depending on the phase difference between the heating and corrugation patterns. The most intense convection and the largest drift occur for wavelengths comparable to the slot height, and their intensities increase proportionally to the heating intensity as well as proportionally to the corrugation amplitude, with the drift being a very strong function of the phase difference. Convection creates forces at the plates which would cause horizontal displacement of the corrugated plate and deform the corrugations if such effects were allowed. Tangential forces generated by the uniform heating always contribute to the corrugation buildup while similar forces generated by the periodic heating contribute to the buildup only when the hot spots overlap with the upper part of the corrugation. The processes described above are qualitatively similar for all Prandtl numbers Pr, with the intensity of convection and the magnitude of the drift increasing with a reduction in Pr.

Key words: convection, flow control

1. Introduction

Thermal convection is one of the most common forms of fluid motion. It occurs in many application areas such as heat exchangers, biological systems, weather

† Email address for correspondence: sabtahi4@uwo.ca

https://doi.org/10.1017/jfm.2017.426 Published online by Cambridge University Press

prediction, and convection in the atmosphere, oceans and within the Earth's mantle, among many others. Understanding its characteristics is therefore of the utmost importance.

The character of convection depends on the geometry of the flow system and on the externally imposed thermal conditions. Because of a large range of variability of such conditions, analyses of fundamental aspects of convection have been focused on simple reference cases. One of the best-known reference problems is natural convection in a horizontal slot subject to a spatially homogeneous heating applied at the lower plate. This problem is referred to as Rayleigh–Bénard (RB) convection (Bénard 1900; Rayleigh 1916) and has been studied for many decades using both theoretical and experimental approaches (Bodenschatz, Pesch & Ahlers 2000). Convection results from the transition from a conductive state when the critical conditions are exceeded (Chilla & Schumacher 2012) and it changes the character of the heat flow in qualitative terms. These critical conditions are expressed in terms of the critical Rayleigh number Ra, with secondary flow occurring for $Ra < Ra_{cr}$. RB convection has the form of rolls (striped pattern) and is characterized by a linear neutral stability curve with a well-defined minimum which identifies the critical Rayleigh number and the critical wave vector, with the onset conditions being independent of the Prandtl number Pr. Explicit estimates for the maximum heat transfer have recently been provided (Hassanzadeh, Chini & Doering 2014). The use of more intense heating leads to secondary bifurcations and the onset of either the skewed-varicose instability, the Eckhaus instability, or the zigzag instability (Clever & Busse 1974; Busse & Clever 1979) described using the so-called Busse balloon. Linear stability theory does not offer any guidelines regarding the spontaneous pattern selection which, in most experiments, is determined by secondary effects. A large enough heating intensity leads to turbulent RB convection (Ahlers, Grossmann & Lohse 2009; Lohse & Xia 2010; Toppaladoddi, Succi & Wettlaufer 2015). Effects of geometric non-uniformities on such convection have been subject to recent studies (Goluskin & Doering 2016).

Inhomogeneities in the plate geometry can affect the onset conditions (McCoy *et al.* 2008; Seiden *et al.* 2008; Weiss, Seiden & Bodenschatz 2012). The detailed analyses and identification of the relevant mechanisms are not available. Two-dimensional convection rolls have been observed for subcritical conditions ($Ra < Ra_{cr}$) for the lower plate being augmented with thin stripes. The amplitude of these rolls grew with Ra until they were destabilized by mechanisms which depended on the ratio between the wavenumber of the imposed modulation and the critical wavenumber of the RB convection, producing a variety of three-dimensional patterns (McCoy *et al.* 2008; Seiden *et al.* 2008). Experiments show that the combined effect of strips parallel to the flow and gravity-induced shear flow leads to the creation of longitudinal and transverse rolls depending on the angle of the corrugation and gravity component (Weiss *et al.* 2012). Recent studies have shown that the conduction-only state does not exist in the presence of geometric modulations, and a natural convection sets in regardless of the heating intensity (Abtahi & Floryan 2017). The properties of this convection are expected to have a strong effect on the secondary states.

Temperature non-uniformities also affect the onset conditions (Freund, Pesch & Zimmermann 2011) as well as create their own convection, which occurs regardless of the heating intensity (Hossain, Floryan & Floryan 2012; Hossain & Floryan 2015*a*,*b*, 2017). As there is an uncountable number of heating non-uniformities, recent studies have been focused on the simplest pattern, consisting of sinusoidal heating with an arbitrary wavelength, and have led to the concept of structured

https://doi.org/10.1017/jfm.2017.426 Published online by Cambridge University Press

convection. There are numerous examples of such convection, e.g. circulation in urban environments as local heating rates are determined by the dissimilar thermal properties of roofs, streets and parks, and circulation in rural environments, where variations of the heating rates of forests, fields and lakes drive the local circulation. Convection within the Earth's mantle is affected by the insulating effect of continents and represents spatially structured convection with heating from above (Lenardic *et al.* 2005). A system of fractures, leads and polynyas in sea ice leads to convection in both the ocean and atmosphere (Marcq & Weiss 2012). The use of mixed insulating and conducting boundary conditions leads to spatially patterned convection (Ripesi *et al.* 2014). Human activity resulting in the heat island effect (Rizwam, Dennis & Liu 2008) can be analysed from the heating pattern point of view. Dynamics of systems of localized fires and prediction of their propagation represent another challenging problem (Finney *et al.* 2012) similar to that of thermal patterning in microfluidic devices (Krishnan, Ugaz & Burns 2002; Beltrame *et al.* 2011). Applying the same heating either from above or from below results in similar motions (Hossain & Floryan 2014). The flow topology is locked in with the heating pattern but only for small convection intensities. Higher intensities result in a transition to secondary states which might have different patterns (Hossain & Floryan 2013*a*).

Heating non-uniformities represent a wider class of problems which has been studied on a case by case basis. The non-uniformities create horizontal and vertical temperature gradients which result in horizontal density variations which create motions frequently referred to as horizontal convection. Maxworthy (1997) has reviewed the numerical and experimental analyses focused on convection in regions with either open or partially open lateral boundaries. Three typical geometries have been considered in this review, i.e. convection in a channel, convection from a patch or strip into stratified and/or rotating surroundings, and convection into a rotating coastal environment. Siggers, Kerswell & Balmforth (2004) have showed numerically that horizontal convection can be unsteady and turbulent, capable of maintaining overturning circulation within a layer heated and cooled differentially at its surface with a general temperature distribution imposed at the top of the layer and a variety of thermal boundary conditions at the base of the layer. Hughes & Griffiths (2008) used horizontal convection as an idealized model of the ocean overturning circulation, where the inhomogeneous profiles of heating were imposed at a horizontal boundary. Horizontal convection in oceans was studied by Winters & Young (2009) from the energy balance point of view, resulting in the conclusion that the buoyancy force alone is insufficient to account for the observed levels of kinetic energy in oceans, and additional energy sources, e.g. wind, are needed.

The simultaneous presence of heating and geometric irregularities results in their potential interactions. As their distributions are characterized in terms of spatial patterns, this leads to the problem of pattern interactions. The irregularities represent external forcing which can be imposed independently. Each pattern has its own characteristics, with their relative position representing an additional parameter. The objective of this study is to evaluate the effect of each forcing introduced both individually and simultaneously, and to provide an assessment of the effects associated with pattern interactions. In § 2 we describe the problem formulation involving the two simplest patterns, i.e. sinusoidal corrugation combined with sinusoidal heating. Since it is known that the system response depends on the Prandtl number (Hossain & Floryan 2013*b*), we focus our discussion on $Pr = 0.72$. Section 3 discusses characteristics of typical convective flows resulting from changes in the relative positions of both patterns. Section 4 provides a detailed analysis of

https://doi.org/10.1017/jfm.2017.426 Published online by Cambridge University Press

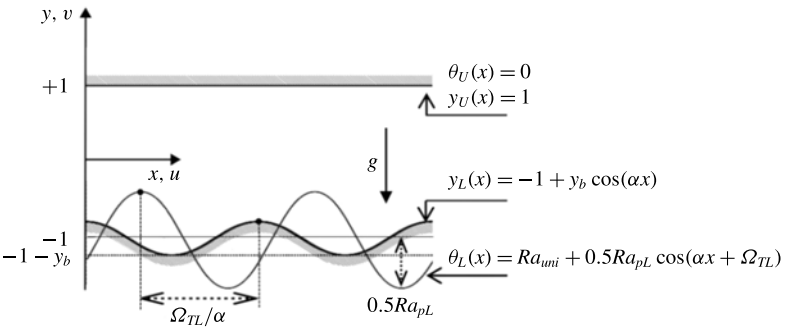


FIGURE 1. Schematic diagram of the flow system.

convective effects for the long-wavelength non-uniformities. Section 5 is focused on non-uniformities with arbitrary wavelengths; § 5.1 discusses convection driven by a purely periodic heating, § 5.2 describes what happens when the geometric and heating non-uniformities are transferred from the lower to the upper plate, and § 5.3 discusses the system response when the uniform and periodic heating components are combined. Section 6 provides an assessment of how variations of Pr affect the system response. Section 7 gives a short summary of the main conclusions.

2. Problem formulation

Consider a slot formed by two horizontal plates, the upper one being smooth and the lower one being corrugated (see figure 1), whose geometry has the following form:

$$y_L^*(x^*) = -h^* + C_L^* \cos(\alpha^* x^*), \quad y_U^*(x^*) = h^*. \tag{2.1a,b}$$

In the above, the subscripts L and U refer to the lower and upper plates, respectively, C_L^* is the corrugation amplitude, α^* is the corrugation wavenumber and stars denote dimensional quantities. The slot is periodic with a wavelength $\lambda^* = 2\pi/\alpha^*$ and extends to $\pm\infty$ in the x-direction, with $2h^*$ being the mean distance between the plates. The gravitational acceleration g^* acts in the negative y-direction, the fluid is incompressible, Newtonian, and has thermal conductivity k^*, specific heat c^*, thermal diffusivity $\kappa^* = k^*/\rho^* c^*$, kinematic viscosity ν^*, dynamic viscosity μ^*, thermal expansion coefficient Γ^* and variations of the density ρ^* follow the Boussinesq approximation.

The upper plate is kept isothermal at temperature T_U^*, which serves as the reference temperature, while the lower plate is subjected to a spatially distributed heating resulting in a sinusoidal distribution of its temperature (T_L^*), i.e.

$$T_L^*(x^*) = T_{mean,L}^* + 0.5 T_{p,L}^* \cos(\alpha^* x^* + \Omega_{TL}^*), \quad T_U^*(x^*) = T_U^*, \tag{2.2a,b}$$

where $T_{p,L}^*$ is the peak-to-peak amplitude of the periodic component and Ω_{TL}^* is the phase shift between the heating and corrugation patterns.

We define the relative temperature as $\theta^* = T^* - T_U^*$ which leads to the plates' temperatures of the form

$$\theta_L^*(x) = \theta_{uni}^* + 0.5\theta_{p,L}^* \cos(\alpha^* x^* + \Omega_{TL}^*), \quad \theta_U^*(x) = 0, \tag{2.3a,b}$$

https://doi.org/10.1017/jfm.2017.426 Published online by Cambridge University Press

where $\theta^*_{uni} = T^*_{mean,L} - T^*_U$, $\theta^*_{p,L} = T^*_{p,L}$. Use of the half of the mean slot height h^* as the length scale and $\kappa^*\nu^*/(g^*\Gamma^* h^{*3})$ as the temperature scale result in the following expressions for the geometry and temperatures

$$y_L(x) = -1 + y_b \cos(\alpha x), \quad y_U(x) = 1, \tag{2.4a,b}$$

$$\theta_L(x) = Ra_{uni} + 0.5 Ra_{p,L} \cos(\alpha x + \Omega_{TL}), \quad \theta_U(x) = 0, \tag{2.4c,d}$$

where y_b is the amplitude of the corrugation, $Ra_{uni} = g^*\Gamma^* h^{*3}\theta^*_{uni}/(\kappa^*\nu^*)$ and $Ra_{pL} = g^*\Gamma^* h^{*3}\theta^*_{p,L}/(\kappa^*\nu^*)$ are the uniform and periodic Rayleigh numbers measuring the intensity of the uniform and periodic heating component.

The field equations consist of the continuity, Navier–Stokes and energy equations of the form

$$\frac{\partial u}{\partial x} + \frac{\partial v}{\partial y} = 0, \quad u\frac{\partial u}{\partial x} + v\frac{\partial u}{\partial y} = -\frac{\partial p}{\partial x} + \nabla^2 u, \tag{2.5a,b}$$

$$u\frac{\partial v}{\partial x} + v\frac{\partial v}{\partial y} = -\frac{\partial p}{\partial y} + \nabla^2 v + Pr^{-1}\theta, \quad u\frac{\partial \theta}{\partial x} + v\frac{\partial \theta}{\partial y} = Pr^{-1}\nabla^2\theta, \tag{2.5c,d}$$

where (u, v) are the velocity components in the (x, y) directions, respectively, scaled with $U^*_v = \nu^*/h^*$ as the velocity scale, p stands for the pressure scaled with $\rho^* U^{*2}_v$ as the pressure scale and $Pr = \nu^*/\kappa^*$ is the Prandtl number. The relevant boundary conditions have the form

$$u(y_L) = u(1) = 0, \quad v(y_L) = v(1) = 0, \quad \theta(y_L) = \theta_L(x), \quad \theta(1) = 0. \tag{2.6a–d}$$

There is no externally imposed horizontal pressure gradient, i.e.

$$\left.\frac{\partial p}{\partial x}\right|_{mean} = 0. \tag{2.7}$$

System (2.5)–(2.7) is solved by expressing the velocity components using the stream function ψ defined in the usual manner, i.e. $u = \partial\psi/\partial y$, $v = -\partial\psi/\partial x$, eliminating pressure and using Fourier expansions in the x-direction and Chebyshev expansions in the y-direction discretization combined with the immersed boundary conditions (IBC) method (Husain & Floryan 2010; Abtahi, Hossain & Floryan 2016) to account for the irregularity of the flow domain. The pressure field is normalized with condition $p(0, 0) = C$, where C represents an arbitrary constant.

The net flow rate Q in the horizontal direction is defined as

$$Q = \int_{y_L(x)}^{y_U(x)} u(x, y)\, \mathrm{d}y. \tag{2.8}$$

The surface stresses acting on the fluid at the lower plate ($\boldsymbol{\sigma}_L$) can be expressed as

$$\boldsymbol{\sigma}_L = \begin{bmatrix}\sigma_{x,L}, & \sigma_{y,L}\end{bmatrix} = \begin{bmatrix} n_{x,L}, & n_{y,L} \end{bmatrix} \begin{bmatrix} \tau_{xx} - p & \tau_{xy} \\ \tau_{yx} & \tau_{yy} - p \end{bmatrix}_{y_L}, \tag{2.9}$$

https://doi.org/10.1017/jfm.2017.426 Published online by Cambridge University Press

where

$$\tau_{xx} = 2\frac{\partial u}{\partial x}, \quad \tau_{xy} = \tau_{yx} = \frac{\partial u}{\partial y} + \frac{\partial v}{\partial x}, \quad \tau_{yy} = 2\frac{\partial v}{\partial y}, \tag{2.10a–c}$$

denote viscous components of the stress tensor and

$$[n_{x,L}, n_{y,L}] = N_L[-\alpha y_b \sin(\alpha x), -1] \tag{2.11}$$

are components of the normal unit vector with $N_L = [1 + (\alpha y_b \sin(\alpha x))^2]^{-1/2}$. The x- and y-components of surface stresses are

$$\sigma_{x,L} = \sigma_{xv,L} + \sigma_{xp,L} = N_L \left[-2\alpha y_b \sin(\alpha x)\frac{\partial u}{\partial x} - \left(\frac{\partial u}{\partial y} + \frac{\partial v}{\partial x}\right)\right]_{y_L} + N_L[\alpha y_b \sin(\alpha x)p]_{y_L}, \tag{2.12a}$$

$$\sigma_{y,L} = \sigma_{yv,L} + \sigma_{yp,L} = N_L \left[-\alpha y_b \sin(\alpha x)\left(\frac{\partial u}{\partial y} + \frac{\partial v}{\partial x}\right) - 2\frac{\partial v}{\partial y}\right]_{y_L} + N_L[p]_{y_L}, \tag{2.12b}$$

where $\sigma_{xv,L}$, $\sigma_{yv,L}$ are generated by viscous effects while $\sigma_{xp,L}$, $\sigma_{yp,L}$ are generated by pressure. Forces acting on the fluid per unit length in the x-direction are

$$F_{x,L} = F_{xv,L} + F_{xp,L} = \lambda^{-1}\int_0^\lambda (\sigma_{xv,L} + \sigma_{xp,L})N_L^{-1}\,\mathrm{d}x, \tag{2.13a}$$

$$F_{y,L} = F_{yv,L} + F_{yp,L} = \lambda^{-1}\int_0^\lambda (\sigma_{yv,L} + \sigma_{yp,L})N_L^{-1}\,\mathrm{d}x. \tag{2.13b}$$

Similar relations can be developed for the upper plate. The corresponding conduction problem has been solved when necessary using methods described in Husain & Floryan (2007).

3. Flow patterns

Typical flow patterns created by convection are displayed in figure 2. Figure 2(*a*,*c*,*e*) displays flow resulting from the hot spots at the lower wall overlapping with the corrugation peaks ($\Omega_{TL} = 0$). The resulting topology consists of pairs of counter-rotating rolls with the fluid moving upwards above the hot spots. Figure 2(*b*,*d*,*f*) displays patterns for $\Omega_{TL} = \pi/2$ with the flow topology consisting of sets of rolls separated from each other by a stream tube weaving up and down and carrying fluid in the positive x-direction. All upper rolls rotate in the same direction and all lower rolls rotate in the direction opposite to the direction of the upper rolls.

In the next section, we begin detailed description of the mechanics of convection by starting with an analytic solution for the long-wavelength system.

4. The long-wavelength system

We begin detailed description of the mechanics of convection by starting with the long-wavelength system, i.e. $\alpha \to 0$. Solution begins with domain transformation of the form

$$\xi = \alpha x, \quad \eta = 2\frac{y-1}{2 - y_b\cos\xi} + 1, \tag{4.1a,b}$$

https://doi.org/10.1017/jfm.2017.426 Published online by Cambridge University Press

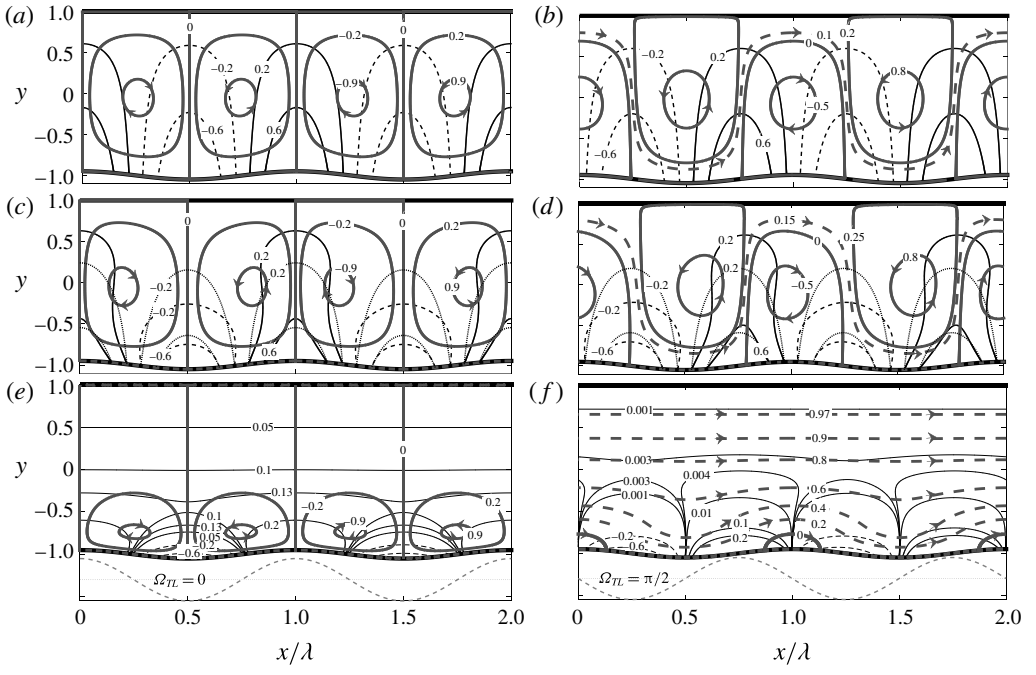


FIGURE 2. The flow (thick solid lines for the individual rolls and thick dashed lines for the stream tube) and the temperature (thin solid lines for the positive values and dashed lines for the negative values) fields for $Ra_{pL} = 400$, $Ra_{uni} = 0$, $y_b = 0.05$ and $\alpha = 0.01,\ 1.22,\ 8$ for $\Omega_{TL} = 0$ (a,c,e) and for $\Omega_{TL} = \pi/2$ (b,d,f). ψ has been normalized with its maxima; $|\psi|_{max} = 0.0591,\ 2.9634,\ 0.0351$ in (a,c,e) and $0.0718,\ 3.6305,\ 0.1886$ in (b,d,f) for $\alpha = 0.01,\ 1.22,\ 8$, respectively. Temperature has been normalized with $\theta_{max} = Ra_{pL}/2$. Dotted lines show conductive isotherms but which are different from the complete isotherms only for $\alpha = 1.22$. Dashed lines illustrate temperatures of the lower plate.

where ξ is a slow scale and η maps the corrugated slot into a regular strip $\eta \in [-1,\ 1]$. The unknowns are represented as power expansions in terms of α of the form

$$[u,\ v,\ \theta] = [u_0,\ v_0,\ \theta_0] + \alpha[u_1,\ v_1,\ \theta_1] + \alpha^2[u_2,\ v_2,\ \theta_2] + O(\alpha^3), \tag{4.2a}$$

$$p = \alpha^{-1}p_{-1} + p_0 + \alpha p_1 + O(\alpha^2), \quad Q = Q_0 + \alpha Q_1 + \alpha^2 Q_2 + O(\alpha^3), \tag{4.2b,c}$$

these expansions are substituted into the field equations, the leading-order systems are extracted and solved with details given in appendix A. The solutions have the following forms:

$$\left.\begin{gathered} u_0 = 0, \quad v_0 = 0, \quad p_{-1} = 0, \\ \theta_0 = Ra_{uni}\tfrac{1}{2}(1-\eta) + Ra_{PL}\tfrac{1}{4}(1-\eta)(\cos\Omega_{TL}\cos\xi - \sin\Omega_{TL}\sin\xi), \quad Q_0 = 0, \end{gathered}\right\} \tag{4.3}$$

https://doi.org/10.1017/jfm.2017.426 Published online by Cambridge University Press

$$\left.\begin{aligned}
&v_1 = 0, \quad \theta_1 = 0,\\
&u_1 = Ra_{uni}Pr^{-1}\sum_{n=0}^{3} LS_{u1,n}\sin(n\xi)\\
&\qquad + Ra_{pL}Pr^{-1}\sum_{n=0}^{3}[KS_{u1,n}\cos\Omega_{TL}\sin(n\xi) + KC_{u1,n}\sin\Omega_{TL}\cos(n\xi)],\\
&p_0 = Ra_{uni}Pr^{-1}[L_{p0} + LC_{p0,1}\cos(\xi)]\\
&\qquad + Ra_{pL}Pr^{-1}\sum_{n=0}^{2}[KS_{p0,n}\sin\Omega_{TL}\sin(n\xi) + KC_{p0,n}\cos\Omega_{TL}\cos(n\xi)] + C,\\
&Q_1 = Ra_{PL}Pr^{-1}K_{Q1}\sin\Omega_{TL},
\end{aligned}\right\} \tag{4.4}$$

$$\left.\begin{aligned}
&u_2 = 0, \quad P_1 = 0,\\
&v_2 = Ra_{uni}Pr^{-1}\sum_{n=0}^{4} LC_{v2,n}\cos(n\xi) + Ra_{pL}Pr^{-1}\sum_{n=0}^{4}[KS_{v2,n}\sin\Omega_{TL}\sin(n\xi)\\
&\qquad + \cos\Omega_{TL}\cos(n\xi)],\\
&\theta_2 = Ra_{uni}Pr^{-1}\sum_{n=0}^{5} L1C_{\theta2,n}\cos(n\xi) + Ra_{uni}^2Pr^{-1}\sum_{n=0}^{5} L2C_{\theta2,n}\cos(n\xi)\\
&\qquad + Ra_{pL}Pr^{-1}\sum_{n=0}^{6}[K1S_{\theta2,n}\sin\Omega_{TL}\sin(n\xi) + K1C_{\theta2,n}\cos\Omega_{TL}\cos(n\xi)]\\
&\qquad + Ra_{pL}^2Pr^{-1}\sum_{n=0}^{6}[K2S_{\theta2,n}\sin\Omega_{TL}\sin(n\xi) + K2C_{\theta2,n}\cos\Omega_{TL}\cos(n\xi)],\\
&Q_2 = 0,
\end{aligned}\right\} \tag{4.5}$$

with all coefficients defined in appendix A.

The structure of (4.3)–(4.5) demonstrates that in the limit of $Ra_{pL} \to 0$ the boundaries between the rolls overlap with the peaks and bottoms of the corrugation (Abtahi & Floryan 2017). Taking an additional limit of $y_b \to 0$ eliminates convection altogether if $Ra_{uni} < 213.5$ (Chandrasekhar 1961). In the limit of $Ra_{uni} \to 0$, $y_b \to 0$ the locations of the boundaries overlap with the locations of the hot and cold spots at the lower wall (Hossain & Floryan 2013*a*, 2016; Asgarian, Hossain & Floryan 2016). The same happens in the corrugated slot, as long as y_b remains small enough, which is of interest in this analysis. This fact can be shown by looking at the flow structure close to the upper plate (see figure 2) where the flow field can be approximated by taking advantage of the simplifications available in the limit of $\eta \to 1$, i.e.

$$\begin{aligned}
u_1(\eta) \;=\; &-\frac{(\eta-1)}{15}y_bPr^{-1}Ra_{uni}\sin\xi\\
&+\frac{(\eta-1)}{15}Pr^{-1}Ra_{pL}\left[-\frac{1}{8}y_b\sin\Omega_{TL} - \sin(\Omega_{TL}+\xi) + \frac{1}{2}y_b\sin(\Omega_{TL}+2\xi)\right]\\
&+O[(\eta-1)^2],
\end{aligned} \tag{4.6}$$

and searching for locations of zeros of the above expression. In the special cases of $\Omega_{TL} = 0$, π, borders between rolls overlap with the peaks and bottoms of the corrugation, which also overlap with the hot and cold spots.

https://doi.org/10.1017/jfm.2017.426 Published online by Cambridge University Press

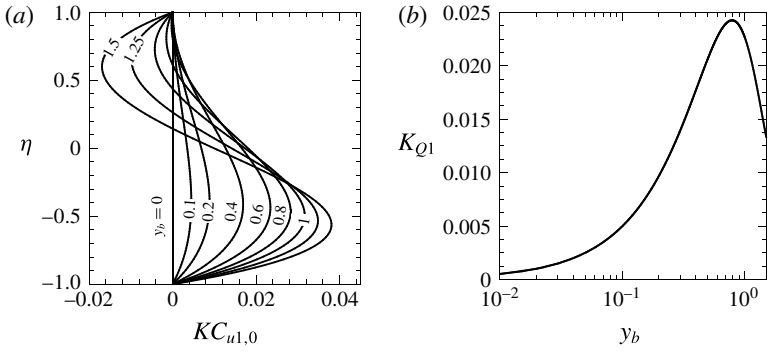


FIGURE 3. Distributions of the aperiodic component of the horizontal velocity, i.e. function $KC_{u1,0}$ (*a*) and variations of Q (function K_{Q1}) as a function of y_b (*b*) for the long-wavelength systems.

Equation (4.4) demonstrates that the velocity field has an aperiodic component in the horizontal direction, but only if there is a phase difference between the corrugation and heating patterns and this phase difference is not equal to $n\pi$, where n is an integer. The vertical distribution of this component is described by the function $KC_{u1,0}$ (see figure 3) and the corresponding volumetric flow rate is in general non-zero. We shall refer to the flow rate carried by this component as the thermal drift. The drift is independent of Ra_{uni}, its magnitude is proportional to Ra_{pL}, Pr^{-1} and $\sin \Omega_{TL}$, and it disappears in the limit of $y_b \to 0$ as well as in the limit of $Ra_{pL} \to 0$ (see (4.4)), i.e. the presence of both the corrugation and the periodic heating is required for its generation. The drift disappears for $\Omega_{TL} = 0, \pi$ and changes direction when Ω_{TL} traverses through any of these points. Since the drift is proportional to $\sin \Omega_{TL}$, this provides a simple means for control of its strength and direction through changes of the relative position of both patterns. The increase of the corrugation height initially increases the drift, but its excessive magnitude generates backflow near the upper plate (see figure 3) and reduces the flow rate.

Figure 4 illustrates evolution of the flow field in response to changes of Ω_{TL}. When $\Omega_{TL} = 0$, the flow field consists of counter-rotating rolls with no mean flow in the horizontal direction, as the hot spots overlap with the corrugation peaks (figure 4*a*). A jetting motion in the positive x-direction appears when $\Omega_{TL} = \pi/4$, with the jet located close to the upper plate for $x \approx (-0.1\lambda, 0.3\lambda)$, then turning rapidly downwards at $x \approx 0.35\lambda$ and staying close to the lower plate for $x \approx (0.4\lambda, 0.8\lambda)$ and, finally, turning up at $x \approx 0.85\lambda$ and staying close to the upper plate (see figure 4*b*). The upward movement of the jet overlaps with the location of the hot spot and the downward movement overlaps with the location of the cold spot. The jet expands when Ω_{TL} increases up to $\Omega_{TL} = \pi/2$ and it occupies the complete cross-sections at $x \approx 0.25\lambda$, 0.75λ with a nearly parabolic distribution of the horizontal velocity component (see figure 4*c*). Further increase of Ω_{TL} results in a decrease of the size of the jet and a change in the locations of the downward and upward turns, as illustrated in figure 4(*d*) for $\Omega_{TL} = 3\pi/4$; the former turn is now located at $x \approx 0.15\lambda$ and the latter at $x \approx 0.65\lambda$. The jet disappears altogether at $\Omega_{TL} = \pi/2$, with the flow consisting of rolls rotating in the directions opposite to that found for $\Omega_{TL} = 0$ (see figure 4*e*).

Appearance of the drift raises a question regarding the origin of forces responsible for its creation. As there is no mean horizontal pressure gradient, i.e. (2.7), the driving

https://doi.org/10.1017/jfm.2017.426 Published online by Cambridge University Press

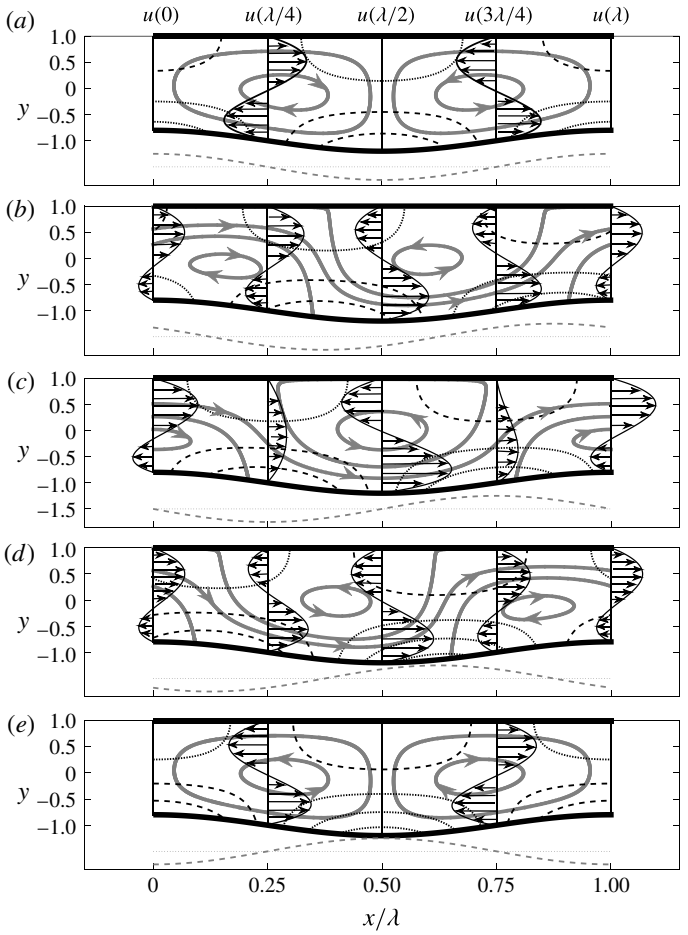


FIGURE 4. Evolution of the flow field as a function of Ω_{TL} for $y_b = 0.2$, $Ra_{pL} = 400$, $Ra_{uni} = 0$, $\alpha \to 0$. (*a–e*) Display results for $\Omega_{TL} = 0, \pi/4, \pi/2, 3\pi/4, \pi$, respectively. Thick solid lines identify streamlines. Thin dashed and dotted lines identify positive and negative pressures. Grey dashed–dotted line below each subfigure illustrates temperatures of the lower wall.

forces must be created at the plates. The upper plate is smooth and can only provide shear force which always opposes fluid movement. The lower plate generates both shear and pressure forces, with the former opposing the fluid movement. One can conclude that it is the pressure force which drives the mean horizontal flow.

Expressions for the x-components of stresses acting on the fluid at both plates are given in appendix A. Their integration over one corrugation wavelength results in the following expressions for the forces acting on the fluid

$$F_{xv,L} = -\alpha y_b Pr^{-1} Ra_{pL} \sin \Omega_{TL} k_{22} + O(\alpha^3), \quad F_{xp,L} = \alpha y_b Pr^{-1} Ra_{pL} \sin \Omega_{TL} k_{23} + O(\alpha^3), \tag{4.7a,b}$$

$$F_{xv,U} = -\alpha y_b Pr^{-1} Ra_{pL} \sin \Omega_{TL} k_{24} + O(\alpha^3), \quad F_{xp,U} = 0, \tag{4.7c,d}$$

https://doi.org/10.1017/jfm.2017.426 Published online by Cambridge University Press

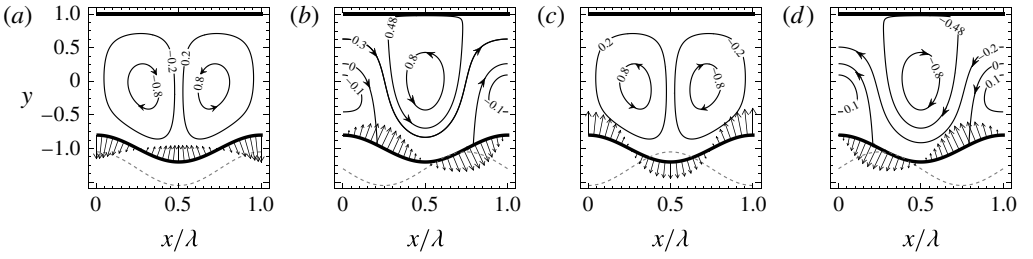


FIGURE 5. Distributions of pressure at the lower plate for $\alpha \to 0$, $y_b = 0.2$, $Ra_{pL} = 400$, $Ra_{uni} = 0$ and $\Omega_{TL} = 0, \pi/2, \pi, 3\pi/2$ in (*a–d*), respectively.

where the coefficients k_{22}, k_{23}, k_{24} are defined in appendix A and are positive for $y_b < 1$. The above expressions demonstrate that the pressure represents the driving force which is opposed by viscous friction.

It is instructive to show in detail how the horizontal pressure force is created. The reader may note that the position of the corrugation is fixed but the position of the heating pattern is dictated by Ω_{TL}. Previous discussion shows that the location of the flow pattern is determined by the position of the heating pattern, and this location shifts in the horizontal direction when Ω_{TL} changes. The process of changing the relative position of the pressure field with respect to the corrugation is illustrated in figure 5, which displays distributions of the pressure along the bottom plate. The reader may note that the direction of the drift changes from right to left due to changes of Ω_{TL} (see figure 5(*b*,*d*) for $\Omega_{TL} = \pi/2$ and $3\pi/2$).

The evaluation of the horizontal pressure force, i.e.

$$\begin{aligned} F_{xp,L} &= \alpha(2\pi)^{-1} y_b \int_0^{2\pi} \sin\xi p_0|_{\eta=-1}\,\mathrm{d}\xi \\ &= \alpha(2\pi Pr)^{-1} y_b Ra_{uni} \int_0^{2\pi} \sin\xi [L_{p0} + LC_{p0,1}\cos\xi]_{\eta=-1}\,\mathrm{d}\xi \\ &\quad + \alpha(2\pi Pr)^{-1} y_b Ra_{pL} \int_0^{2\pi} \sin\xi \sum_{n=0}^{2} [KS_{p0,n}\sin\Omega_{TL}\sin(n\xi) \\ &\quad + KC_{p0,n}\cos\Omega_{TL}\cos(n\xi)]_{\eta=-1}\,\mathrm{d}\xi \\ &\quad + \alpha(2\pi)^{-1} C y_b \int_0^{2\pi} \sin\xi\,\mathrm{d}\xi, \end{aligned} \tag{4.8}$$

shows that it can be viewed as a projection of the pressure field onto the geometry. This force has been referred to as the pressure interaction drag in the analysis of drag formation in grooved channels (Mohammadi & Floryan 2012), but it acts as a propulsive force in the present case as it is created by an external effect, i.e. by the heating. Orthogonality properties of trigonometric functions lead to the final expression, which is identical to (4.7*b*).

Shifting the relative position of the pressure field with respect to the corrugations results in different projections, different horizontal forces and different mean flow rates. The most effective projection resulting in the largest force and the largest drift corresponds to $\Omega_{TL} = \pm\pi/2$. The reader may note that a more complex corrugation geometry would lead to a more complex projection for the same heating pattern.

https://doi.org/10.1017/jfm.2017.426 Published online by Cambridge University Press

The horizontal forces at the upper and lower plates act in the opposite directions and this would lead to the relative movement of these plates if horizontal displacements were permitted. There would be no limit to the magnitude of this displacement as the force is dictated by the relative position of corrugation and heating pattern, which are unaltered by the plate movement; thus, the movement would persist as long as $\Omega_{TL} \neq 0, \pi$.

The horizontal forces acting on both sides of a single corrugation 'bump' are not the same and this may lead to 'bump' deformation if the plate was made of a soft material, e.g. biological membrane. Forces acting on the left ($\hat{H}_{x,L(left)}$) and right ($\hat{H}_{x,L(right)}$) sides of a single 'bump' are defined as

$$\left.\begin{aligned}\hat{H}_{x,L(left)} &= -2\lambda^{-1}\int_{-\lambda/2}^{0}(\sigma_{xv,L}+\sigma_{xp,L})N_L^{-1}\,\mathrm{d}x\\ &= \frac{\alpha}{5\pi Pr}[-y_b k_{25}Ra_{uni}+Ra_{pL}(k_{26}\cos\Omega_{TL}-k_{27}\sin\Omega_{TL})],\\ \hat{H}_{x,L(right)} &= 2\lambda^{-1}\int_{0}^{\lambda/2}(\sigma_{xv,L}+\sigma_{xp,L})N_L^{-1}\,\mathrm{d}x\\ &= \frac{\alpha}{5\pi Pr}[-y_b k_{25}Ra_{uni}+Ra_{pL}(k_{26}\cos\Omega_{TL}+k_{27}\sin\Omega_{TL})],\end{aligned}\right\} \quad (4.9a,b)$$

where the hat symbol has been added to mark forces acting on the plate as opposed to forces acting on the fluid, and all coefficients are defined in appendix A. Positive $\hat{H}_{x,L(left)}$ and $\hat{H}_{x,L(right)}$ are directed into the 'bump' and the difference between them defines the deforming force $\widehat{DF}_{x,L}$, i.e.

$$\begin{aligned}\widehat{DF}_{x,L} &= \hat{H}_{x,L(left)}-\hat{H}_{x,L(right)}\\ &= -2\lambda^{-1}\int_{-\lambda/2}^{\lambda/2}(\sigma_{xv,L}+\sigma_{xp,L})N_L^{-1}\,\mathrm{d}x=-2(F_{xp,L}+F_{xv,L})\\ &= -2F_{x,L}=2\hat{F}_{x,L}=-\frac{2\alpha}{5\pi Pr}k_{27}Ra_{pL}\sin\Omega_{TL}\approx -0.05\frac{\alpha}{Pr}y_b Ra_{pL}\sin\Omega_{TL},\end{aligned} \quad (4.10)$$

which is equal and opposite to twice the net force acting on the fluid and is generated by the periodic heating.

We shall now inquire if the shear force would contribute to the corrugation buildup assuming erosion was allowed. This question is relevant as an accidental creation of a surface ripple could lead to its uncontrolled growth. Integration of tangential stress gives the total shear forces acting on the left ($\hat{H}_{t,L(left)}$) and right ($\hat{H}_{t,L(right)}$) sides of a single 'bump' (see appendix A for details). Positive $\hat{H}_{t,L(left)}$ and $\hat{H}_{t,L(right)}$ are directed towards the 'bump' peak which signals the tendency for the corrugation growth. We shall use simplified expressions valid for $y_b \to 0$, i.e.

$$\left.\begin{aligned}\hat{H}_{t,L(right)} &= \frac{\alpha}{5\pi Pr}[y_b Ra_{uni}+Ra_{pL}(\cos\Omega_{TL}+2.356y_b\sin\Omega_{TL})],\\ \hat{H}_{t,L(left)} &= \frac{\alpha}{5\pi Pr}[y_b Ra_{uni}+Ra_{pL}(\cos\Omega_{TL}-2.356y_b\sin\Omega_{TL})],\end{aligned}\right\} \quad (4.11a,b)$$

which show that the uniform heating always contributes to the buildup. The periodic heating contributes only if the hot spots overlap with the upper part of the corrugation.

https://doi.org/10.1017/jfm.2017.426 Published online by Cambridge University Press

Since only $Ra_{uni} < 213.5$ is of interest in this analysis, the periodic part of the heating determines if the convection contributes to the buildup. It is interesting to note that $\hat{H}_{t,L(left)}$ and $\hat{H}_{t,L(right)}$ are not equal.

The above solution provides an acceptable accuracy for $\alpha < 0.1$ as determined through comparisons with the complete solution (details not shown).

5. Systems with an arbitrary wavenumber

The mechanics of convective processes has been explained in the previous section. We shall now inquire how the system responds when its wavelengths are comparable to the slot height. The relevant solutions have been obtained using a spectrally accurate numerical solution of the complete model equations (2.5)–(2.7) with the algorithm details given in (Husain & Floryan 2010; Abtahi *et al.* 2016). The discussion begins with a purely periodic heating.

5.1. *Slot exposed to a purely periodic heating* ($Ra_{uni} \to 0$)

Results displayed in figure 2 demonstrate that the heating wavelength determines the topology of the flow field similarly as in the smooth slot (Hossain & Floryan 2013*b*). The rolls completely fill in the slot for long wavelengths (see in figure 2*a*,*b*) but convection is very weak (see figure 6). Reduction of the wavelength down to $\alpha = 1.22$ (see in figure 2*c*,*d*) results in an intensification of convection (see figure 6) with the rolls still completely filling in the slot. Further reduction of the wavelength down to $\alpha = 8$ (see in figure 2*e*,*f*) results in a weakening of convection (see figure 6) with the fluid movement limited to a boundary layer adjacent to the corrugated plate; the thickness of this boundary layer rapidly decreases with increasing α. Addition of a phase shift between the heating and corrugation patterns adds a stream tube carrying the fluid in the horizontal direction (compare figure 2*a–f*). The stream tube expands as α increases and it occupies around 90 % of slot volume at $\alpha = 8$. There are two processes associated with convection and they lead to different values of $|\psi|_{max}$ (see figure 6). The first process is associated with rotation of rolls and locations of the corresponding $|\psi|_{max}$ overlaps with roll centres. The second process is associated with the formation of the stream tube and the relevant $|\psi|_{max}$ are located at the upper wall and their values give the flow rate Q. Analysis carried out in § 4 shows that $|\psi|_{max}$ associated with the roll motion is dominant with $|\psi|_{max} = 0(\alpha)$ for $\alpha \to 0$. At the same time, $Q = 0(\alpha)$, but only if $\Omega_{TL} \neq 0, \pi$, as $Q = 0$ in these two special cases. Numerical estimates carried out for $\alpha \to \infty$ (see Floryan & Floryan (2015), for methodology) show that $|\psi|_{max}$ associated with the roll motion decreases proportionally to α^{-3} until it becomes small enough that it is overcome by $|\psi|_{max}$ associated with the formation of the stream tube. From that moment on, $|\psi|_{max}$ decreases at a rate proportional to α^{-1}, as $Q = 0(\alpha^{-1})$ (see figure 6). The stream tube is not formed for $\Omega_{TL} = 0, \pi$ and in this case $|\psi|_{max} = 0(\alpha^{-3})$. The maxima of $|\psi|_{max}$ and Q occur at different values of α and Ω_{TL}; in the case of conditions used in figures 6 and 7 they occur at $(\alpha, \Omega_{TL}) \approx (0.86, \pi/2), (1.22, \pi/2)$, respectively.

The convection intensity, as measured by $|\psi|_{max}$, as well as the net flow rate Q, display nearly sinusoidal variations as functions of Ω_{TL} (see figure 7*a*), including the change of direction of Q between $\Omega_{TL} \in (0, \pi)$ and $\Omega_{TL} \in (\pi, 2\pi)$. The maxima of $|\psi|_{max}$ occur approximately at $\Omega_{TL} = \pi/2, 3\pi/2$, which also correspond to the maxima of Q. Both $|\psi|_{max}$ and Q increase proportionally to Ra_{pL}, with a small reduction of the growth rate observed for $Ra_{pL} > 10^3$ suggesting the beginning of a saturation process (see figure 7*b*). The effect of an increase in y_b is best represented by looking at the

https://doi.org/10.1017/jfm.2017.426 Published online by Cambridge University Press

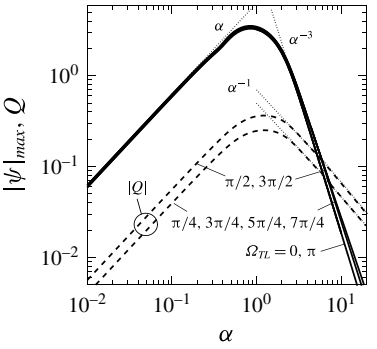


FIGURE 6. Variations of $|\psi|_{max}$ and Q as functions of α for $Ra_{pL} = 400$, $Ra_{uni} = 0$, $y_b = 0.02$. Thin dotted lines mark asymptotes. The maxima of $|\psi|_{max}$ and Q occur at $(\alpha, \Omega_{TL}) \approx (0.86, \pi/2), (1.22, \pi/2)$.

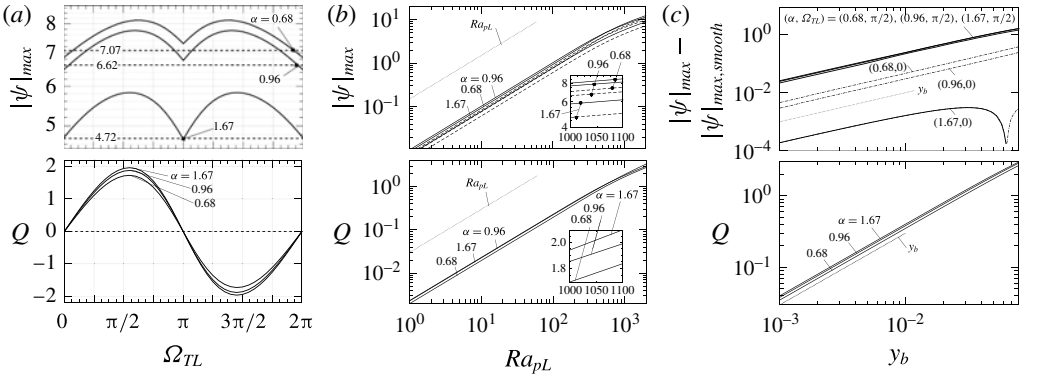


FIGURE 7. Variations of $|\psi|_{max}$ and Q as functions of Ω_{TL} (a), Ra_{pL} (b) and y_b (c). The results are for $Ra_{uni} = 0$, $Pr = 0.71$, $y_b = 0.05$, $\Omega_{TL} = \pi/2$, $Ra_{pL} = 1000$ unless specified otherwise in the figure. Dashed lines correspond to the smooth slot and dotted lines identify various asymptotes. Dashed–dotted lines in (c) identify negative values. Wavenumbers $\alpha = 0.68$, 1.67 produce maxima of $|\psi|_{max}$, Q, respectively.

change with respect to convection in a smooth slot ($y_b \to 0$) (Hossain & Floryan 2013*a*). The proper test quantity is thus $|\psi|_{max} - |\psi|_{max,smooth}$ for the stream function and Q for the flow rate as $Q_{smooth} = 0$. Results displayed in figure 7(c) demonstrate a linear growth of both the convection intensity and the flow rate with y_b for the range of corrugation amplitudes being of interest. This conclusion is supported by results of the analysis of the small-y_b limit analysis presented in appendix B.

The effect of the phase difference is well illustrated in figure 8 for the range of α producing the strongest convection. The results show that $|\psi|_{max}$ and Q can be significantly altered by changing Ω_{TL}. The maxima of these quantities do not occur for the same conditions, e.g. the maximum of $|\psi|_{max}$ and the maximum of Q occur at $(\alpha, \Omega_{TL}) \approx (0.86, \pi/2), (1.22, \pi/2)$, respectively, for flow conditions used in the lowerhalf of figure 8. Increasing Ra_{pL} from 400 to 1000 and y_b from 0.02 to 0.05

https://doi.org/10.1017/jfm.2017.426 Published online by Cambridge University Press

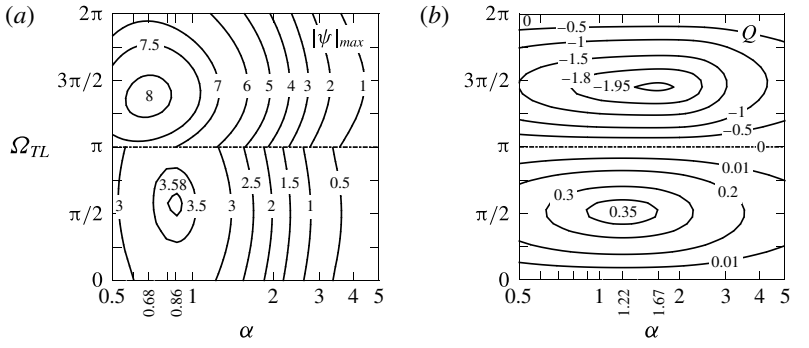


FIGURE 8. Variations of $|\psi|_{max}$ (*a*) and Q (*b*) as functions of α and Ω_{TL} for $Ra_{pL} = 400$, $Ra_{uni} = 0$, $y_b = 0.02$ in the lower half of these figures and for $Ra_{pL} = 1000$, $y_b = 0.05$ in the upper half. Results can be extended to the full range of Ω_{TL} by taking advantage of the periodicity in the Ω_{TL}-direction.

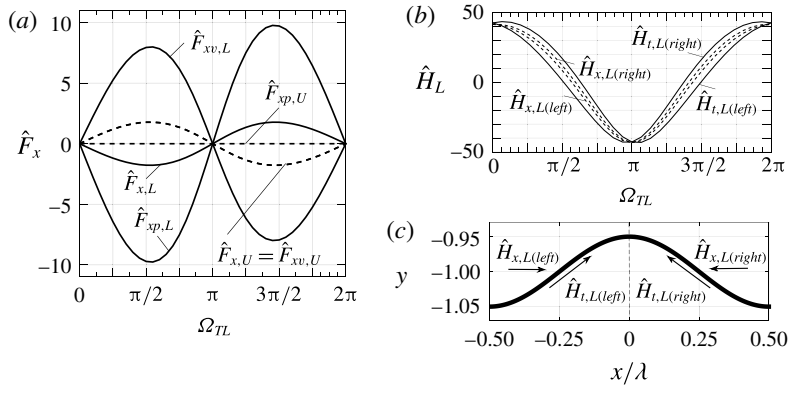


FIGURE 9. Variations of the x-component of forces acting on the plates (*a*; see (2.13) for definition) and forces acting on the right and left sides of the corrugation (*b*; see (4.9*a*,*b*)–(4.11*a*,*b*) for definitions) as functions of Ω_{TL} for $\alpha = 1.67$, $y_b = 0.05$, $Ra_{pL} = 1000$, $Ra_{uni} = 0$. In (*a*), solid (dashed) lines correspond to the lower (upper) plate. Hats above symbols signify forces acting on the plates. Directions of forces acting on the corrugation are shown in (*c*).

moves these maxima to $(\alpha, \Omega_{TL}) \approx (0.68, 2\pi/3)$, $(1.67, \pi/2)$, respectively (see the upper half of figure 8).

Variations of forces acting on the plates as functions of Ω_{TL} are illustrated in figure 9. Forces at each plate act in opposite directions, which may result in a relative horizontal translation of the plates if such an effect was permitted. There is no limit to the magnitude of such translation as forces persist as long as $\Omega_{TL} \neq 0, \pi$. The forces acting per one wavelength may not be large, but could become significant if integrated over several wavelengths. The same forces would contribute to the horizontal deformation of the corrugation if such an effect was allowed.

https://doi.org/10.1017/jfm.2017.426 Published online by Cambridge University Press

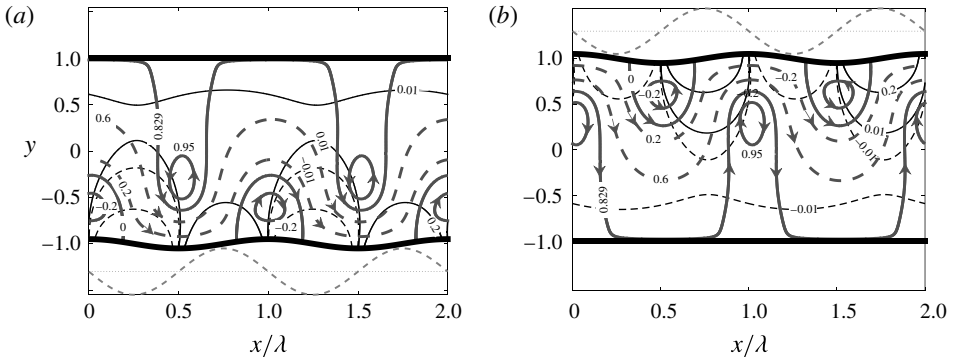


FIGURE 10. The flow and temperature fields for $Ra_{uni} = 0$, $\Omega_{TL} = \pi/2$ for heating and corrugations placed at the lower plate (a; $Ra_{pL} = 400$, $Ra_{pU} = 0$, $\alpha = 4$, $y_b = 0.05$, $y_t = 0$) and at the upper plate (b; $Ra_{pL} = 0$, $Ra_{pU} = 400$, $\alpha = 4$, $y_b = 0$, $y_t = 0.05$). Thick solid, thick dashed, thin solid and thin dashed lines identify streamlines, stream tubes, positive isotherms and negative isotherms, respectively. ψ and θ are normalized with their maxima; $|\psi|_{max} = 0.5131$, $\theta_{max} = Ra_{pL}/2$ for the lower plate heating and $\theta_{max} = Ra_{pU}/2$ for the upper plate heating. Dashed line below (a) illustrates temperature of the lower plate while dashed line above (b) illustrates temperature of the upper plate.

5.2. *Placement of the corrugation and the heating at the upper plate*

We shall now move the corrugations as well as the periodic heating to the upper plate. The proper boundary conditions have the following form

$$u(-1) = u(y_U) = 0, \quad v(-1) = v(y_U) = 0, \tag{5.1a,b}$$

$$\theta(-1) = 0, \quad \theta(y_U) = \theta_U(x) = 0.5 Ra_{pU} \cos(\alpha x + \Omega_{TU}), \tag{5.1c,d}$$

where $y_U(x) = 1 + y_t \cos(\alpha x)$ and the field equations remain unchanged (see (2.5)). The resulting convection is analogous to convection resulting from the heating and corrugations placed at the lower plate. This similarity can be demonstrated by (i) reversing the direction of gravity, i.e. $Ra_{pU} \to -Ra_{pL}$, and (ii) changing the sign of the temperature, i.e. $\theta \to -\theta$ (Hossain & Floryan 2014). The latter condition implies a change of the sign of the temperature imposed at the lower plate and results in a shift of the temperature field by half of a cycle in the x-direction. This similarity is illustrated in figure 10.

5.3. *Effects of the uniform heating*

We shall now return the corrugations and the heating to the lower plate and investigate changes associated with introduction of the uniform heating/cooling component. The topology of the flow field is not affected. Increasing Ra_{uni} increases both $|\psi|_{max}$ and Q nearly linearly (see figure 11a). Cooling of the lower plate, which corresponds to negative values of Ra_{uni}, decrease $|\psi|_{max}$ and Q also almost linearly. The most intense convection occurs for $\alpha = O(1)$ and it decreases rapidly for $\alpha \to 0$ and $\alpha \to \infty$ always in the same manner regardless of the value of Ra_{uni} (see figure 11b). Intensity of convection changes in the same manner as a function of Ω_{TL} for all values of Ra_{uni} while the amplitudes of variation of both $|\psi|_{max}$ and Q increase significantly with increasing Ra_{uni} and decrease with negative values of Ra_{uni} (see figure 12a). Both $|\psi|_{max}$ and Q increase proportionally to y_b above the level found in the case of a smooth slot (see figure 12b).

https://doi.org/10.1017/jfm.2017.426 Published online by Cambridge University Press

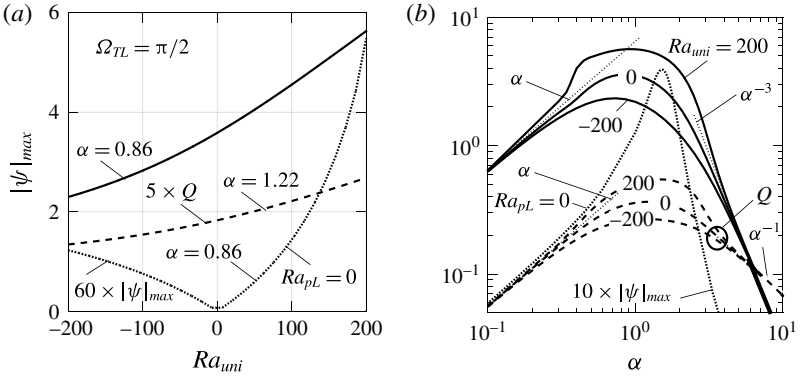


FIGURE 11. Variations of $|\psi|_{max}$ (solid lines), and Q (dashed lines) as functions of Ra_{uni} for (α, Ω_{TL}) values which maximize them (*a*) and as functions of α for $\Omega_{TL} = \pi/2$ (*b*). All results are for $y_b = 0.02$, $Ra_{pL} = 400$. Dotted lines describe a purely uniform heating ($Ra_{pL} = 0$, $Ra_{uni} = 200$). Thin dotted lines identify various asymptotes.

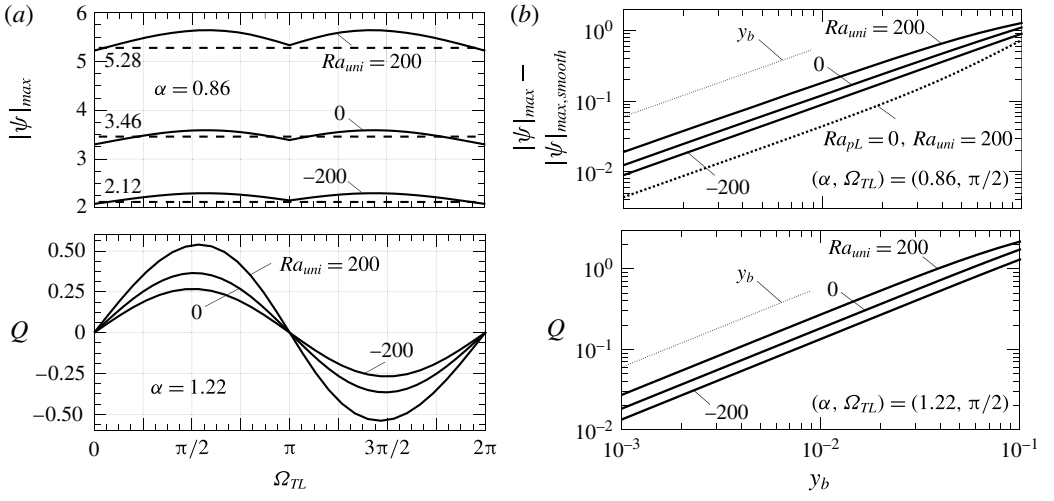


FIGURE 12. Variations of $|\psi|_{max}$ and Q as functions of Ω_{TL} for $y_b = 0.02$, $Ra_{pL} = 400$ (*a*) and as functions of y_b for $Ra_{pL} = 400$ and (α, Ω_{TL}) values which maximize them (*b*). Dashed lines provide data for the smooth slot. Dotted line in figure 13(*b*) provides data for a purely uniform heating ($Ra_{pL} = 0$, $Ra_{uni} = 200$). Thin dotted lines identify various asymptotes. A purely uniform heating with $Ra_{uni} = 200$ results in $|\psi|_{max} = 0.0914$.

6. Effects of Prandtl number

All results presented in the previous sections have been obtained for $Pr = 0.71$. A decrease of the Prandtl number leads to an increase of the horizontal temperature gradients, which results in an increase of the intensity of convection, i.e. increases of $|\psi|_{max}$ and Q (see figure 13*a*). The most intense convection occurs for $\alpha = O(1)$ and decreases rapidly for $\alpha \to 0$ and $\alpha \to \infty$ in the same manner for all values of Pr (see figure 13*b*). Convection intensity changes also in the same manner as a function of Ω_{TL} (figure 14*a*), while the amplitudes of variation of both $|\psi|_{max}$ and Q increase significantly with a reduction in Pr (figure 14*b*).

https://doi.org/10.1017/jfm.2017.426 Published online by Cambridge University Press

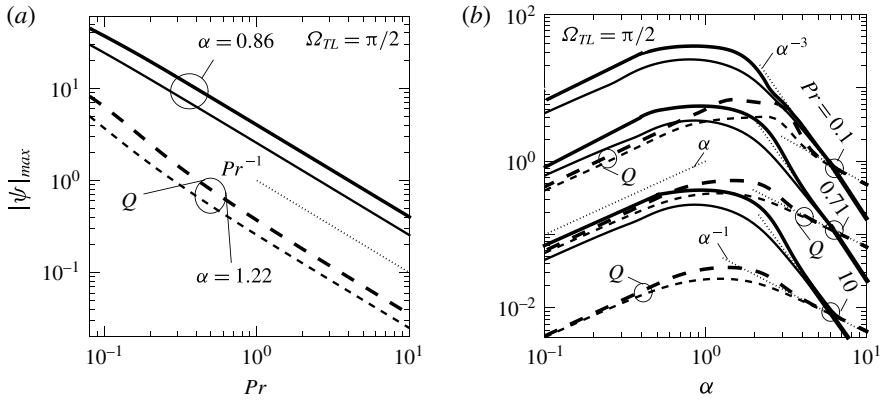


FIGURE 13. Variations of $|\psi|_{max}$ (solid lines), and Q (dashed lines) as functions of Pr for $\Omega_{TL} = \pi/2$ and α values which maximize them when $Pr = 0.71$ (a) and as functions of α (b) for $y_b = 0.02$, $Ra_{pL} = 400$. Thick and thin solid (dashed) lines correspond to $Ra_{uni} = 200$, 0, respectively. Thin dotted lines identify various asymptotes.

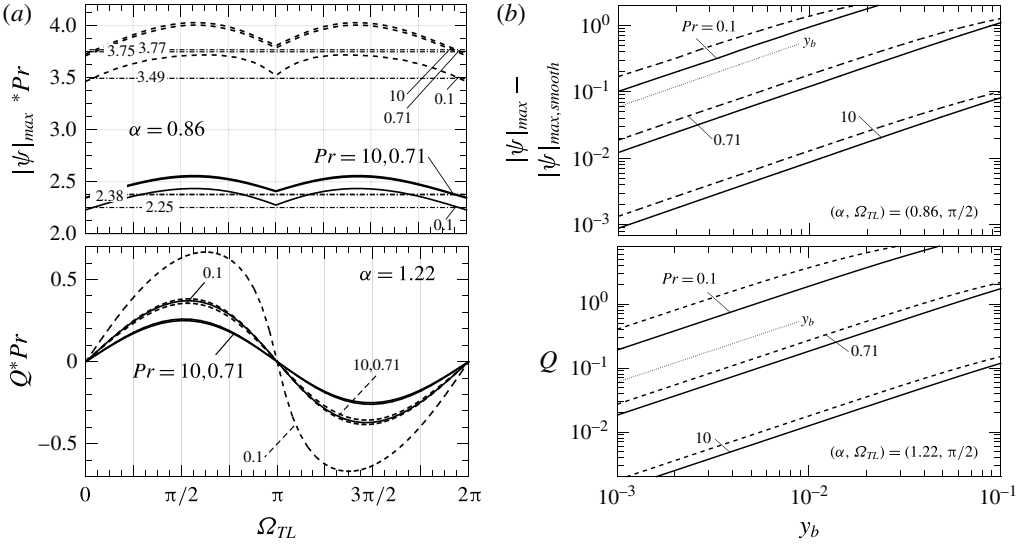


FIGURE 14. Variations of $|\psi|_{max}$, and Q as functions of Ω_{TL} for $y_b = 0.02$ (a) and as functions of y_b for (α, Ω_{TL}) values which maximize them when $Pr = 0.71$ (b). In all cases, $Ra_{pL} = 400$, $Ra_{uni} = 0$ (solid lines) and $Ra_{uni} = 200$ (dashed lines). Dashed–dotted lines provide data for the smooth slot. Thin dotted lines identify various asymptotes.

7. Conclusions

An analysis of natural convection in a horizontal fluid layer exposed to heating and geometric non-uniformities has been carried out. The layer is bounded from above by a smooth plate and from below by a corrugated plate. The analysis considered the geometrically simplest case, i.e. sinusoidal corrugation characterized by the wavenumber α and the amplitude y_b. The upper plate is kept isothermal while the lower plate is exposed to a spatially non-uniform heating. The heating non-uniformities resulted in the lower plate's temperature consisting of a superposition

https://doi.org/10.1017/jfm.2017.426 Published online by Cambridge University Press

of a mean part different from that of the upper plate and a sinusoidal component. The heating intensity due to the difference between the mean temperature of the plates is expressed in terms of the uniform Rayleigh number Ra_{uni}, while the amplitude of the sinusoidal component is expressed in terms of the periodic Rayleigh number Ra_{pL}. The spatial distribution of the periodic component is characterized by the same wavenumber α as the corrugation geometry, and its relative position with respect to the corrugation is expressed in terms of the phase difference Ω_{TL}, with $\Omega_{TL} = 0, \pi$ resulting in the overlap of the hot spots with the corrugation tips and troughs, respectively. The analysis is limited to heating conditions which do not give rise to secondary motions in the absence of all non-uniformities. It utilizes a spectrally accurate numerical solution as well as an analytic solution for the long-wavelength non-uniformities.

The heating creates horizontal temperature gradients which lead to the formation of vertical and horizontal pressure gradients which drive the motion regardless of the intensity of the heating. When the hot spots overlap either with the corrugation tips or with the corrugation bottoms, convection assumes the form of pairs of counter-rotating rolls whose size is dictated by the heating/corrugation wavelengths. Misalignment of the hot spots and corrugation peaks results in the formation of a net horizontal flow referred to as thermal drift. This flow can be directed in the positive as well as in the negative horizontal directions depending on the phase difference between the heating and corrugation patterns. It has been shown that both periodic heating as well as periodic corrugations are required for the formation of such flow. The force driving this flow is created through the projection of the convective pressure field onto the plate geometry. The most intense convection and the largest flow occur for the non-uniformities' with wavelengths comparable to the slot height, with their strength rapidly decreasing when $\alpha \to 0$ and $\alpha \to \infty$. It has also been shown that the intensity of convection and the magnitude of the thermal drift increase proportionally to the heating intensity. This increase slows down for more intense heating due to the increase of the strength of nonlinear effects and flow saturation. Similarly, the intensity increases linearly with the corrugation amplitude but, eventually, the growth begins to slow due to the increase of friction associated with the increase of the plate area. An increase of the uniform heating component magnifies the above effects while cooling reduces them. Transferring the corrugation and periodic heating to the upper plate results in a similar convection if the up/down symmetries are taken into account.

The question of whether or not convection created by an accidental creation of surface ripples can create forces supporting further changes in the slot geometry has been considered. It has been shown that convection creates forces which would cause horizontal displacement of the corrugated plate and would deform the corrugations. Tangential forces generated by the uniform heating always contribute to the corrugation buildup while similar forces generated by the periodic heating contribute to the buildup only when locations of the hot spots overlap with the upper part of the corrugation.

The process described above is qualitatively similar for all Prandtl numbers, with the intensity of convection and the magnitude of the drift increasing with a reduction in Pr. The presence of geometric and heating non-uniformities is expected to affect the transition conditions for secondary convection. This problem is yet to be investigated.

Acknowledgements

This work has been carried out with the support of NSERC of Canada.

https://doi.org/10.1017/jfm.2017.426 Published online by Cambridge University Press

Appendix A. Solution of the convection problem in the long-wavelength limit ($\alpha \to 0$)

The solution process begins with domain transformation of the form

$$\xi = \alpha x, \quad \eta = 2\frac{y-1}{2-y_b\cos\xi} + 1, \tag{A 1a,b}$$

where ξ is a slow scale and η maps the corrugated slot into a regular strip $\eta \in [-1, 1]$. The field equations expressed in the (ξ, η)-coordinates take the form

$$\alpha\frac{\partial u}{\partial \xi} + F_7\frac{\partial u}{\partial \eta} + F_8\frac{\partial v}{\partial \eta} = 0, \tag{A 2a}$$

$$\frac{\partial^2 u}{\partial \eta^2} + [F_1 - F_2 u - F_3 v]\frac{\partial u}{\partial \eta} + F_4\frac{\partial^2 u}{\partial \xi\,\partial \eta} + F_5\frac{\partial^2 u}{\partial \xi^2} - F_6 u\frac{\partial u}{\partial \xi} - F_6\frac{\partial p}{\partial \xi} - F_2\frac{\partial p}{\partial \eta} = 0, \tag{A 2b}$$

$$\frac{\partial^2 v}{\partial \eta^2} + [F_1 - F_2 u - F_3 v]\frac{\partial v}{\partial \eta} + F_4\frac{\partial^2 v}{\partial \xi\,\partial \eta} + F_5\frac{\partial^2 v}{\partial \xi^2} - F_6 u\frac{\partial v}{\partial \xi} - F_3\frac{\partial p}{\partial \eta} + Pr^{-1}F_9\theta = 0, \tag{A 2c}$$

$$\frac{\partial^2 \theta}{\partial \eta^2} + [F_1 - PrF_2 u - PrF_3 v]\frac{\partial \theta}{\partial \eta} + F_4\frac{\partial^2 \theta}{\partial \xi\,\partial \eta} + F_5\frac{\partial^2 \theta}{\partial \xi^2} - PrF_6 u\frac{\partial \theta}{\partial \xi} = 0, \tag{A 2d}$$

where

$$\left.\begin{gathered} F_1 = \frac{\eta_{xx}}{\eta_x^2+\eta_y^2} = \alpha^2\frac{2y_b^2\sin^2\xi - y_b G\cos\xi}{4}(\eta-1) + O(\alpha^4), \\ F_2 = \frac{\eta_x}{\eta_x^2+\eta_y^2} = -\alpha\frac{y_b G\sin\xi}{4}(\eta-1) + O(\alpha^3), \\ F_3 = \frac{\eta_y}{\eta_x^2+\eta_y^2} = \frac{G}{2} - \alpha^2\frac{y_b^2 G\sin^2\xi}{8}(\eta-1)^2 + O(\alpha^4), \\ F_4 = \frac{2\alpha\eta_x}{\eta_x^2+\eta_y^2}, \quad F_5 = \frac{\alpha^2}{\eta_x^2+\eta_y^2} = \alpha F_6, \\ F_6 = \frac{\alpha}{\eta_x^2+\eta_y^2} = \alpha\frac{G^2}{4} + O(\alpha^3), \quad F_7 = \eta_x = -\alpha\frac{y_b\sin\xi}{G}(\eta-1), \quad F_8 = \eta_y = \frac{2}{G}, \\ F_9 = \frac{1}{\eta_x^2+\eta_y^2} = \frac{G^2}{4} - \alpha^2\frac{y_b^2 G^2\sin^2\xi}{16}(\eta-1)^2 + O(\alpha^4), \quad G = 2 - y_b\cos\xi. \end{gathered}\right\} \tag{A 3}$$

The boundary conditions and the pressure gradient constraint after transformation take the following form:

$$\left.\begin{gathered} u(\xi, \pm 1) = 0, \quad v(\xi, \pm 1) = 0, \\ \theta(\xi, -1) = Ra_{uni} + 0.5Ra_{pL}\cos(\xi + \Omega_{TL}), \quad \theta(\xi, 1) = 0, \\ \left[\alpha\frac{\partial p}{\partial \xi} - \alpha\frac{y_b(\eta-1)\sin\xi}{2-y_b\cos\xi}\frac{\partial p}{\partial \eta}\right]_{mean} = 0. \end{gathered}\right\} \tag{A 4}$$

The unknowns are represented as power expansions in terms of α, i.e.

$$\left.\begin{gathered} [u, v, \theta] = [u_0, v_0, \theta_0] + \alpha[u_1, v_1, \theta_1] + \alpha^2[u_2, v_2, \theta_2] + O(\alpha^3), \\ p = \alpha^{-1}p_{-1} + p_0 + \alpha p_1 + O(\alpha^2), \quad Q = Q_0 + \alpha Q_1 + \alpha^2 Q_2 + O(\alpha^3), \end{gathered}\right\} \tag{A 5}$$

https://doi.org/10.1017/jfm.2017.426 Published online by Cambridge University Press

these expansions are substituted into (A.2)–(A 4) and the three leading-order systems are extracted:

$$O(1): \frac{\partial v_0}{\partial \eta} = 0, \quad \frac{\partial^2 u_0}{\partial \eta^2} - \frac{G}{2} v_0 \frac{\partial u_0}{\partial \eta} - \frac{1}{4} G^2 \frac{\partial p_{-1}}{\partial \xi} + \frac{1}{4} y_b G \sin\xi (\eta - 1) \frac{\partial p_{-1}}{\partial \eta} = 0, \tag{A 6a,b}$$

$$\frac{\partial p_{-1}}{\partial \eta} = 0, \quad \frac{\partial^2 \theta_0}{\partial \eta^2} - Pr \frac{G}{2} v_0 \frac{\partial \theta_0}{\partial \eta} = 0, \tag{A 6c,d}$$

$$\left.\begin{gathered} u_0(\xi, \pm 1) = 0, \quad v_0(\xi, \pm 1) = 0, \\ \theta_0(\xi, -1) = Ra_{uni} + 0.5 Ra_{pL} \cos(\xi + \Omega_{TL}), \quad \theta_0(\xi, 1) = 0, \\ \left[\frac{\partial P_{-1}}{\partial \xi} - \frac{y_b(\eta - 1)\sin\xi}{2 - y_b \cos\xi} \frac{\partial P_{-1}}{\partial \eta}\right]_{mean} = 0. \end{gathered}\right\} \tag{A 6e}$$

$$O(\alpha^1): \frac{\partial v_1}{\partial \eta} = 0, \quad \frac{\partial^2 u_1}{\partial \eta^2} - \frac{1}{4} G^2 \frac{\partial p_0}{\partial \xi} + \frac{y_b G \sin\xi}{4} (\eta - 1) \frac{\partial p_0}{\partial \eta} = 0, \tag{A 7a,b}$$

$$-\frac{G}{2} \frac{\partial p_0}{\partial \eta} + \frac{G^2}{4Pr} \theta_0 = 0, \quad \frac{\partial^2 \theta_1}{\partial \eta^2} - \frac{PrG}{2} v_1 \frac{\partial \theta_0}{\partial \eta} = 0, \tag{A 7c,d}$$

$$\left.\begin{gathered} u_1(\xi, \pm 1) = 0, \quad v_1(\xi, \pm 1) = 0, \quad \theta_1(\xi, \pm 1) = 0, \\ \left[\frac{\partial P_0}{\partial \xi} - \frac{y_b(\eta - 1)\sin\xi}{2 - y_b \cos\xi} \frac{\partial P_0}{\partial \eta}\right]_{mean} = 0. \end{gathered}\right\} \tag{A 7e–h}$$

$$O(\alpha^2): \frac{\partial v_2}{\partial \eta} - \frac{y_b \sin\xi}{2} (\eta - 1) \frac{\partial u_1}{\partial \eta} + \frac{G}{2} \frac{\partial u_1}{\partial \xi} = 0, \tag{A 8a}$$

$$\frac{\partial^2 u_2}{\partial \eta^2} - \frac{1}{4} G^2 \frac{\partial p_1}{\partial \xi} + \frac{y_b G \sin\xi}{4} (\eta - 1) \frac{\partial p_1}{\partial \eta} = 0, \tag{A 8b}$$

$$-\frac{G}{2} \frac{\partial p_1}{\partial \eta} + \frac{G^2}{4Pr} \theta_1 = 0, \tag{A 8c}$$

$$\begin{aligned} &\frac{\partial^2 \theta_2}{\partial \eta^2} + \frac{2 y_b^2 \sin^2\xi - y_b G \cos\xi}{4} (\eta - 1) \frac{\partial \theta_0}{\partial \eta} + \frac{Pr y_b G \sin\xi}{4} (\eta - 1) u_1 \frac{\partial \theta_0}{\partial \eta} \\ &- \frac{PrG}{2} v_2 \frac{\partial \theta_0}{\partial \eta} - \frac{y_b G \sin\xi}{2} (\eta - 1) \frac{\partial^2 \theta_0}{\partial \eta \partial \xi} \\ &+ \frac{G^2}{4} \frac{\partial^2 \theta_0}{\partial \xi^2} - \frac{PrG^2}{4} u_1 \frac{\partial \theta_0}{\partial \xi} = 0, \end{aligned} \tag{A 8d}$$

$$\left.\begin{gathered} u_2(\xi, \pm 1) = 0, \quad v_2(\xi, \pm 1) = 0, \quad \theta_2(\xi, \pm 1) = 0, \\ \left[\frac{\partial P_1}{\partial \xi} - \frac{y_b(\eta - 1)\sin\xi}{2 - y_b \cos\xi} \frac{\partial P_1}{\partial \eta}\right]_{mean} = 0. \end{gathered}\right\} \tag{A 8e–h}$$

Solutions have forms (4.3)–(4.5) with the relevant coefficients defined as:

$$\left.\begin{aligned} LS_{u1,1} &= \frac{y_b(y_b^2 + 16)}{1536} (\eta^2 - 1) \left(\eta^2 - 4\eta - \frac{1}{5}\right), \\ LS_{u1,2} &= -\frac{y_b^2}{192} (\eta^2 - 1) \left(\eta^2 - 4\eta - \frac{1}{5}\right), \\ LS_{u1,3} &= \frac{y_b^3}{7680} (\eta^2 - 1)(5\eta^2 - 20\eta - 1), \end{aligned}\right\} \tag{A 9}$$

https://doi.org/10.1017/jfm.2017.426 Published online by Cambridge University Press

$$
\left.\begin{aligned}
KC_{u1,0} &= \frac{-5y_b}{7680y_b^6-230\,400y_b^4-737\,280y_b^2-1\,966\,080}(\eta^2-1)\left[\left(\eta^2-4\eta+\frac{8}{5}\right)y_b^8\right.\\
&\quad+(-14\eta^2+56\eta-26)y_b^6+\left(-576\eta^2+2304\eta-\frac{1152}{5}\right)y_b^4\\
&\quad\left.+\left(1792\eta^2+7168\eta+\frac{20\,224}{5}\right)y_b^2-4096\eta^2+16\,384\eta-\frac{69\,632}{5}\right],\\
KS_{u1,1} &= \frac{(y_b^2+16)}{1536}(\eta^2-1)\left(\eta^2-4\eta-\frac{1}{5}\right),\\
KC_{u1,1} &= \frac{55}{7680y_b^6-230\,400y_b^4-737\,280y_b^2-1\,966\,080}(\eta^2-1)\left[\left(\eta^2-4\eta+\frac{223}{55}\right)y_b^8\right.\\
&\quad+\left(-\frac{314}{11}\eta^2+\frac{1256}{11}\eta-10\right)y_b^6+\left(-\frac{1536}{11}\eta^2+\frac{6144}{11}\eta-\frac{5376}{55}\right)y_b^4\\
&\quad\left.+\left(-\frac{4352}{11}\eta^2+\frac{17\,408}{11}\eta+\frac{41\,216}{55}\right)y_b^2-\frac{4096}{11}\eta^2+\frac{16\,384}{11}\eta+\frac{4096}{55}\right],\\
KS_{u1,2} &= -\frac{y_b}{192}(\eta^2-1)\left(\eta^2-4\eta-\frac{1}{5}\right),\\
KC_{u1,2} &= \frac{-5y_b}{7680y_b^6-230\,400y_b^4-737\,280y_b^2-1\,966\,080}(\eta^2-1)\left[\left(\eta^2-4\eta-\frac{19}{5}\right)y_b^8\right.\\
&\quad+\left(-22\eta^2+88\eta-\frac{626}{5}\right)y_b^6+\left(-336\eta^2+1344+\frac{7248}{5}\right)y_b^4\\
&\quad\left.+\left(-1024\eta^2+4096\eta-\frac{8192}{5}\right)y_b^2-2048\eta^2+8192\eta+\frac{2048}{5}\right],\\
KS_{u1,3} &= \frac{1}{7680}(\eta^2-1)(5\eta^2-20\eta-1)y_b^2,\\
KC_{u1,3} &= \frac{5y_b^2}{7680y_b^6-230\,400y_b^4-737\,280y_b^2-1\,966\,080}(\eta^2-1)\left[\left(\eta^2-4\eta-\frac{163}{5}\right)y_b^6\right.\\
&\quad+\left(-30\eta^2+120\eta+\frac{3486}{5}\right)y_b^4\\
&\quad\left.+(-96\eta^2+384\eta-4128)y_b^2-256\eta^2+1024\eta+\frac{256}{5}\right],\\
L_{p0} &= -24y_b^2-8(5\eta^2-10\eta-1)y_b+80\eta^2-160\eta,\\
LC_{p0,1} &= \tfrac{1}{8}y_b\eta^2-2\eta+\tfrac{11}{5},\\
KC_{p0,0} &= \frac{5}{-320+160y_b}\left[(\eta-1)^2y_b^2+\left(-2\eta^2+4\eta-\frac{34}{5}\right)y_b+\frac{8}{5}\right],
\end{aligned}\right\}
$$

(A 9 cont.)

https://doi.org/10.1017/jfm.2017.426 Published online by Cambridge University Press

$$
\begin{aligned}
KS_{p0,1} &= \frac{5}{40y_b^6 - 1200y_b^4 - 3840y_b^2 - 10\,240}\left[\left(\eta^2 - 2\eta + \frac{8}{5}\right)y_b^6\right.\\
&\quad + \left(-30\eta^2 + 60\eta + \frac{318}{5}\right)y_b^4\\
&\quad \left. + \left(-96\eta^2 + 192\eta + \frac{1248}{5}\right)y_b^2 - 256\eta^2 + 512 + \frac{256}{5}\right],\\
KC_{p0,1} &= -\tfrac{1}{8}(\eta^2 - 2\eta - \tfrac{1}{5}),\\
KS_{p0,2} &= \frac{-5y_b}{160y_b^6 - 4800y_b^4 - 15\,360y_b^2 - 40\,960}\left[\left(\eta^2 - 2\eta - \frac{4}{5}\right)y_b^6\right.\\
&\quad + \left(-30\eta^2 + 60\eta - \frac{78}{5}\right)y_b^4\\
&\quad \left. + \left(-96\eta^2 + 192\eta - \frac{1632}{5}\right)y_b^2 - 256(\eta - 1)^2\right],\\
KC_{p0,2} &= \tfrac{1}{32}y_b(\eta - 1)^2,\\
K_{Q1} &= \frac{y_b(15y_b^8 - 80y_b^6 - 768y_b^4 + 6144y_b^2 - 16\,384)}{1280(y_b^6 - 30y_b^4 - 96y_b^2 - 256)},\\
LC_{v2,0} &= \frac{y_b^2(y_b^2 + 16)}{6144}(\eta - 1)(\eta^2 - 1)\left(\eta^2 - 4\eta - \frac{1}{5}\right),\\
LC_{v2,1} &= -y_b\tfrac{13}{7680}(\eta - 1)(\eta^2 - 1)\left[\left(y_b^2 + \tfrac{16}{13}\right)\eta^2 + \left(-4y_b^2 - \tfrac{64}{13}\right) - \tfrac{17}{13}y_b^2 - \tfrac{80}{13}\right],\\
LC_{v2,2} &= \tfrac{1}{7680}y_b^2(\eta - 1)(\eta^2 - 1)(y_b^2\eta^2 - 4y_b^2 - 5y_b^2 + 4\eta^2 - 16\eta - 116),\\
LC_{v2,3} &= \frac{y_b^3}{7680}(\eta - 1)(\eta^2 - 1)(\eta^2 - 4\eta + 43),\\
LC_{v2,4} &= -\frac{y_b^4}{30\,720}(\eta - 1)(\eta^2 - 1)(\eta^2 - 4\eta + 19),\\
KC_{v2,0} &= \frac{y_b(y_b^2 + 16)}{6144}(\eta - 1)(\eta^2 - 1)\left(\eta^2 - 4\eta - \frac{1}{5}\right),\\
KS_{v2,1} &= \frac{-1}{15\,360y_b^6 - 460\,800y_b^4 - 1\,474\,560y_b^2 - 3\,932\,160}(\eta - 1)(\eta^2 - 1)\\
&\quad \times [(\eta^2 - 4\eta + 25)y_b^{10} + (-12\eta^2 + 48\eta + 168)y_b^8\\
&\quad + (-668\eta^2 + 2672\eta - 11\,636)y_b^6 + (-1024\eta^2 + 4096\eta - 2560)y_b^4\\
&\quad + (-1536\eta^2 + 6144\eta - 139\,776)y_b^2 + 8192\eta^2 - 32\,768\eta - 40\,960],\\
KC_{v2,1} &= -\tfrac{13}{7680}(\eta - 1)(\eta^2 - 1)\left[\left(y_b^2 + \tfrac{16}{13}\right)\eta^2 + \left(-4y_b^2 - \tfrac{64}{13}\right)\eta - \tfrac{17}{13}y_b^2 - \tfrac{80}{13}\right],
\end{aligned}
$$

(A 9 cont.)

https://doi.org/10.1017/jfm.2017.426 Published online by Cambridge University Press

$$
\begin{aligned}
KS_{v2,2} &= \frac{9y_b}{15\,360y_b^6 - 460\,800y_b^4 - 1\,474\,560y_b^2 - 3\,932\,160}(\eta-1)(\eta^2-1)\\
&\times\left[\left(\eta^2-4\eta+\frac{91}{3}\right)y_b^8+\left(-\frac{278}{9}\eta^2+\frac{1112}{9}\eta-\frac{4178}{9}\right)y_b^6\right.\\
&+\left(-\frac{208}{3}\eta^2+\frac{832}{3}\eta-\frac{2416}{3}\right)y_b^4+\left(-\frac{512}{3}\eta^2+\frac{2048}{3}\eta-2560\right)y_b^2\\
&\left.+\frac{2048}{9}\eta^2-\frac{8192}{9}\eta-\frac{59\,392}{9}\right],\\
KC_{v2,2} &= \frac{y_b}{7680}(\eta-1)(\eta^2-1)(y_b^2\eta^2-4y_b^2\eta-5y_b^2+4\eta^2-16\eta-116),\\
KS_{v2,3} &= \frac{-y_b^2}{15\,360(\eta-1)(y_b^6-30y_b^4-96y_b^2-256)}(\eta^2-1)\\
&\times[(\eta^4-6\eta^3+16\eta^2-9\eta-20)y_b^8\\
&+(-28\eta^4+168\eta^3-52\eta^2+360\eta-1744)y_b^6\\
&+(-156\eta^4+936\eta^3-11\,568\eta^2+10\,584\eta+20\,940)y_b^4\\
&+(-448\eta^4+2688\eta^3+27\,392\eta^2-14\,976\eta-106\,816)y_b^2\\
&-512(\eta-1)^2(\eta^2-4\eta+43)],\\
KC_{v2,3} &= \frac{y_b^2}{7680}(\eta-1)(\eta^2-1)(\eta^2-4\eta+43),\\
KS_{v2,4} &= \frac{y_b^3}{30\,720(\eta-1)(y_b^6-30y_b^4-96y_b^2-256)}(\eta^2-1)\\
&\times[(\eta^4-6\eta^3+82\eta^2+66\eta-575)y_b^6\\
&+(-30\eta^4+180\eta^3-1992\eta^2-1044\eta+12\,102)y_b^4\\
&+(-96\eta^4+576\eta^3+4224\eta^2+17\,856\eta-77\,856)y_b^2\\
&-256(\eta-1)^2(\eta^2-4\eta+19)],\\
KC_{v2,4} &= -\frac{y_b^3}{30\,720}(\eta-1)(\eta^2-1)(\eta^2-4\eta+19).
\end{aligned}
\qquad \text{(A 9 cont.)}
$$

Coefficients $L1_{\theta 2}, L2_{\theta 2}, L1C_{\theta 2,n}, L2C_{\theta 2,n}, K1_{\theta 2}, K2_{\theta 2}, K1S_{\theta 2,n}, K2S_{\theta 2,n}, K1C_{\theta 2,n}, K2C_{\theta 2,n}$ are not presented due to their length.

The x-components of stresses acting on the fluid at both plates can be expressed as

$$
\begin{aligned}
\sigma_{xv,L} &= \alpha Pr^{-1}(2-y_b\cos\xi)^{-1}\,[k_1\sin\xi+k_2\cos\xi-k_3\sin(2\xi)-k_4\cos(2\xi)\\
&\quad+k_5\sin(3\xi)+k_6\cos(3\xi)-k_7]+O(\alpha^3),
\end{aligned}
\qquad \text{(A 10)}
$$

https://doi.org/10.1017/jfm.2017.426 Published online by Cambridge University Press

$$\sigma_{xp,L} = -\alpha Pr^{-1}\,[k_8 \sin\xi + k_9 \cos\xi + k_{10}\sin(2\xi) + k_{11}\cos(2\xi) - k_{12}\sin(3\xi) - k_{13}\cos(3\xi) - k_{14}] - \alpha C y_b \sin\xi + O(\alpha^3), \tag{A 11}$$

$$\sigma_{xv,U} = -\alpha Pr^{-1}(2 - y_b\cos\xi)^{-1}\,[k_{15}\sin\xi + k_{16}\cos\xi - k_{17}\sin(2\xi) - k_{18}\cos(2\xi) + k_{19}\sin(3\xi) + k_{20}\cos(3\xi) + k_{21}] + O(\alpha^3), \tag{A 12}$$

$$\sigma_{xp,U} = 0, \tag{A 13}$$

with coefficients defined as

$$\left.\begin{aligned}
k_1 &= \frac{y_b^2+16}{80}(y_b Ra_{uni} + Ra_{pL}\cos\Omega_{TL}),\\
k_2 &= \frac{Ra_{pL}\sin\Omega_{TL}}{300(256+96y_b^2+30y_b^4-y_b^6)}[16\,384 + 11\,264y_b^2 + 7296y_b^4 + 1400y_b^6 - 83y_b^8],\\
k_3 &= \frac{y_b}{10}(y_b Ra_{uni} + Ra_{pL}\cos\Omega_{TL}),\\
k_4 &= \frac{y_b Ra_{pL}\sin\Omega_{TL}}{320(256+96y_b^2+30y_b^4-y_b^6)}[8192 + 5632y_b^2 + 192y_b^4 + 196y_b^6 - y_b^8],\\
k_5 &= \frac{y_b^2}{80}(y_b Ra_{uni} + Ra_{pL}\cos\Omega_{TL}),\\
k_6 &= \frac{y_b^2 Ra_{pL}\sin\Omega_{TL}}{320(256+96y_b^2+30y_b^4-y_b^6)}[1024 + 3840y_b^2 - 456y_b^4 + 23y_b^6],\\
k_7 &= \frac{y_b\sin\Omega_{TL} Ra_{pL}}{640(256+96y_b^2+30y_b^4-y_b^6)}[57\,344 + 8192y_b^2 + 5184y_b^4 + 160y_b^6 - 11y_b^8],\\
k_8 &= 5y_b\frac{Ra_{pL}\left(\frac{4}{5} - \frac{22}{5}y_b + y_b^2\right)\cos\Omega_{TL} + \frac{12}{5}Ra_{uni}\left(10 - \frac{14}{3}y_b - y_b^2\right)}{160 - 80y_b},\\
k_9 &= \frac{y_b^2 Ra_{pL}\sin\Omega_{TL}}{320(256+96y_b^2+30y_b^4-y_b^6)}[5120 + 3072y_b^2 + 528y_b^4 - 11y_b^6],\\
k_{10} &= \frac{y_b}{40}(7Ra_{pL}\cos\Omega_{TL} - 13y_b Ra_{uni}),\\
k_{11} &= \frac{y_b Ra_{pL}\sin\Omega_{TL}}{80(256+96y_b^2+30y_b^4-y_b^6)}[3584 + 192y_b^2 + 132y_b^4 - 23y_b^6],\\
k_{12} &= \tfrac{1}{16}y_b^2 Ra_{pL}\cos\Omega_{TL},\\
k_{13} &= \frac{y_b^2 Ra_{pL}\sin\Omega_{TL}}{320(256+96y_b^2+30y_b^4-y_b^6)}[5120 + 3072y_b^2 + 528y_b^4 - 11y_b^6],\\
k_{14} &= \frac{y_b Ra_{pL}\sin\Omega_{TL}}{80(256+96y_b^2+30y_b^4-y_b^6)}y_b Ra_{pL}\sin\Omega_{TL}[3584 + 192y_b^2 + 132y_b^4 - 23y_b^6],\\
k_{15} &= \frac{16+y_b^2}{120}(y_b Ra_{uni} + Ra_{pL}\cos\Omega_{TL}),
\end{aligned}\right\} \tag{A 14}$$

https://doi.org/10.1017/jfm.2017.426 Published online by Cambridge University Press

$$k_{16}=\frac{Ra_{pL}\sin\Omega_{TL}}{960(256+96y_b^2+30y_b^4-y_b^6)}[32\,768+53\,248y_b^2+8832y_b^4+2080y_b^6+29y_b^8],$$
$$k_{17}=\frac{y_b}{15}(Ra_{pL}\cos\Omega_{TL}+y_bRa_{uni}),$$
$$k_{18}=\frac{y_bRa_{pL}\sin\Omega_{TL}}{960(256+96y_b^2+30y_b^4-y_b^6)}[16\,384+3584y_b^2+6144y_b^4-148y_b^6-17y_b^8],$$
$$k_{19}=\frac{y_b^2}{120}(Ra_{pL}\cos\Omega_{TL}+y_bRa_{uni}),$$
$$k_{20}=\frac{y_b^2Ra_{pL}\sin\Omega_{TL}}{960(256+96y_b^2+30y_b^4-y_b^6)}[2048-9600y_b^2+1968y_b^4-89y_b^6],$$
$$k_{21}=\frac{y_bRa_{pL}\sin\Omega_{TL}}{1920(256+96y_b^2+30y_b^4-y_b^6)}[8192-47\,104y_b^2-7488y_b^4-80y_b^6+7y_b^8].$$

(A 14 cont.)

Coefficients used in (4.7*a*,*b*)–(4.9*a*,*b*):

$$k_{22}=\frac{1}{256+96y_b^2+30y_b^4-y_b^6}\left[\frac{768}{5}-\frac{72}{5}y_b^2+\frac{9}{2}y_b^4-\frac{51}{160}y_b^6-\frac{9(16\,384-5120y_b^2+512y_b^4-40y_b^6+y_b^8)}{640\sqrt{4-y_b^2}}\right],$$
$$k_{23}=\frac{1}{256+96y_b^2+30y_b^4-y_b^6}\left[\frac{224}{5}+\frac{12}{5}y_b^2+\frac{33}{20}y_b^4-\frac{23}{80}y_b^6\right],$$
$$k_{24}=\frac{1}{256+96y_b^2+30y_b^4-y_b^6}\left[\frac{608}{5}-\frac{132}{5}y_b^2+\frac{3}{4}y_b^4-\frac{31}{160}y_b^6-\frac{9(16\,384-5120y_b^2+512y_b^4-40y_b^6+y_b^8)}{640\sqrt{4-y_b^2}}\right],$$
$$k_{25}=\frac{26-12y_b-3y_b^2}{4-2y_b},\quad k_{26}=\frac{12-9y_b+19y_b^2-5y_b^3}{12-6y_b},$$
$$k_{27}=\frac{\pi y_b}{128(256+96y_b^2+30y_b^4-y_b^6)}\left[-69\,632+10\,752y_b^2-1824y_b^4+20y_b^6+\frac{147\,456-46\,080y_b^2+4608y_b^4-360y_b^6+9y_b^8}{\sqrt{4-y_b^2}}\right].$$

(A 15)

The tangential stress acting on the lower plate has the following form

$$\begin{aligned}\hat{\sigma}_{t,L}\;=\;&-\alpha Pr^{-1}(2-y_b\cos\zeta)^{-1}Ra_{uni}[k_{28}\sin\xi-k_{29}\sin(2\xi)+k_{30}\sin(3\xi)]\\&-\alpha Pr^{-1}(2-y_b\cos\xi)^{-1}Ra_{pL}\{[k_{31}\sin\xi+k_{32}\sin(2\xi)+k_{33}\sin(3\xi)]\cos\Omega_{TL}\\&+[k_{34}\cos\xi-k_{35}\cos(2\xi)+k_{36}\cos(3\xi)-k_{37}]\sin\Omega_{TL}\}+O(\alpha^3),\end{aligned}\tag{A 16}$$

https://doi.org/10.1017/jfm.2017.426 Published online by Cambridge University Press

with coefficients defined as

$$\left.\begin{gathered} k_{28}=\tfrac{1}{80}y_b(y_b^2+16),\quad k_{29}=\tfrac{1}{10}y_b^2,\quad k_{30}=\tfrac{1}{80}y_b^3,\\ k_{31}=\tfrac{1}{80}(y_b^2+16),\quad k_{32}=\tfrac{1}{10}y_b,\\ k_{33}=\frac{1}{80}y_b^2,\quad k_{34}=\frac{1}{300}\frac{16\,384+11\,264y_b^2+7296y_b^4+1400y_b^6-83y_b^8}{256+96y_b^2+30y_b^4-y_b^6},\\ k_{35}=\frac{1}{320}y_b\frac{8192+5632y_b^2+192y_b^4+196y_b^6-y_b^8}{256+96y_b^2+30y_b^4-y_b^6},\\ k_{36}=\frac{1}{320}y_b^2\frac{1024+3840y_b^2-456y_b^4+23y_b^6}{256+96y_b^2+30y_b^4-y_b^6},\\ k_{37}=\frac{1}{640}y_b\frac{57\,344+8192y_b^2+5184y_b^4+160y_b^6-11y_b^8}{256+96y_b^2+30y_b^4-y_b^6}. \end{gathered}\right\} \tag{A 17}$$

Total shear forces acting on the left ($\hat{H}_{t,L(left)}$) and right ($\hat{H}_{t,L(right)}$) sides of a single 'bump' are expressed as (see figure 9)

$$\left.\begin{aligned} \hat{H}_{t,L(right)}&=-2\lambda^{-1}\int_0^{\lambda/2}\hat{\sigma}_{t,L}N_L^{-1}\,\mathrm{d}x=\frac{\alpha}{5\pi Pr}[y_bRa_{uni}+Ra_{pL}(\cos\Omega_{TL}+k_{38}\sin\Omega_{TL})],\\ \hat{H}_{t,L(left)}&=2\lambda^{-1}\int_{-(\lambda/2)}^{0}\hat{\sigma}_{t,L}N_L^{-1}\,\mathrm{d}x=\frac{\alpha}{5\pi Pr}[y_bRa_{uni}+Ra_{pL}(\cos\Omega_{TL}-k_{38}\sin\Omega_{TL})], \end{aligned}\right\} \tag{A 18}$$

with

$$\begin{aligned} k_{38}\;=\;&\frac{9\pi y_b}{128(256+96y_b^2+30y_b^4-y_b^6)}\left[\frac{32\,768}{3}-1024y_b^2+320y_b^4-\frac{68}{3}y_b^6\right.\\ &\left.-\frac{16\,384-5120y_b^2+512y_b^4-40y_b^6+y_b^8}{\sqrt{4-y_b^2}}\right]. \end{aligned} \tag{A 19}$$

Appendix B. Solution of the convection problem for the small corrugation amplitude ($y_b\to 0$)

The unknowns are represented in the form of power expansions in terms of the corrugation amplitude of the form

$$[u,\,v,\,\theta,\,P]=[u_0,\,v_0,\,\theta_0,\,P_0]+y_b[u_1,\,v_1,\,\theta_1,\,P_1]+O(y_b^2), \tag{B 1}$$

the expansions are substituted into (2.5) and the leading-order terms are extracted, resulting in the following systems:

$$\left.\begin{aligned} O(1):\ &\frac{\partial u_0}{\partial x}+\frac{\partial v_0}{\partial y}=0,\quad \nabla^2u_0-\frac{\partial p_0}{\partial x}-u_0\frac{\partial u_0}{\partial x}-v_0\frac{\partial u_0}{\partial y}=0\\ &\nabla^2v_0-\frac{\partial p_0}{\partial y}-u_0\frac{\partial v_0}{\partial x}-v_0\frac{\partial v_0}{\partial y}+Pr^{-1}\theta_0=0,\\ &Pr^{-1}\nabla^2\theta_0-u_0\frac{\partial\theta_0}{\partial x}-v_0\frac{\partial\theta_0}{\partial y}=0,\quad \left.\frac{\partial P_0}{\partial x}\right|_{mean}=0. \end{aligned}\right\} \tag{B 2}$$

https://doi.org/10.1017/jfm.2017.426 Published online by Cambridge University Press

$$\left.\begin{gathered} O(y_b^1): \frac{\partial u_1}{\partial x}+\frac{\partial v_1}{\partial y}=0, \quad \nabla^2 u_1-\frac{\partial p_1}{\partial x}-u_0\frac{\partial u_1}{\partial x}-u_1\frac{\partial u_0}{\partial x}-v_0\frac{\partial u_1}{\partial y}-v_1\frac{\partial u_0}{\partial y}=0, \\ \nabla^2 v_1-\frac{\partial p_1}{\partial y}-u_0\frac{\partial v_1}{\partial x}-u_1\frac{\partial v_0}{\partial x}-v_0\frac{\partial v_1}{\partial y}-v_1\frac{\partial v_0}{\partial y}+Pr^{-1}\theta_1=0, \\ Pr^{-1}\nabla^2\theta_1-u_1\frac{\partial \theta_0}{\partial x}-u_0\frac{\partial \theta_1}{\partial x}-v_1\frac{\partial \theta_0}{\partial y}-v_0\frac{\partial \theta_1}{\partial y}=0, \quad \left.\frac{\partial P_1}{\partial}\right|_{mean}=0. \end{gathered}\right\} \tag{B 3}$$

Use of (B 1) in the boundary conditions and their transfer to the mean plate position give:

$$\left.\begin{gathered} O(1): y=1: u_0=0, \quad v_0=0, \quad \theta_0=0, \\ y=-1: u_1=0, \quad v_1=0, \quad \theta_0=Ra_{uni}+0.5Ra_{p,L}\cos(\alpha x+\Omega_{TL}), \end{gathered}\right\} \tag{B 4}$$

$$\left.\begin{gathered} O(y_b^1): y=1: u_0=0, \quad v_0=0, \quad \theta_0=0, \\ y=-1: u_1=-\frac{1}{2}\frac{\partial u_0}{\partial y}(e^{i\alpha x}+e^{-i\alpha x}), \quad v_1=-\frac{1}{2}\frac{\partial v_0}{\partial y}(e^{i\alpha x}+e^{-i\alpha x}), \\ \theta_1=-\frac{1}{2}\frac{\partial \theta_0}{\partial y}(e^{i\alpha x}+e^{-i\alpha x}). \end{gathered}\right\} \tag{B 5}$$

Solution of (B 2), (B 4) represents convection in a smooth slot exposed to periodic heating and has a solution in the following functional form (Hossain *et al.* 2012):

$$[u_0, v_0, \theta_0, p_0](x,y)=\sum_{n=-\infty}^{n=+\infty}[U_0^{(n)}(y), V_0^{(n)}(y), \emptyset_0^{(n)}(y), P_0^{(n)}(y)]e^{in(\alpha x+\Omega_{TL})}. \tag{B 6}$$

Substitution of (B 6) into (B 5) results in the following form of boundary conditions at the lower plate:

$$y=-1: [u_1, v_1, \theta_1]=-\tfrac{1}{2}\sum_{n=-\infty}^{n=+\infty}[DU_0^{(n)}, DV_0^{(n)}, D\emptyset_0^{(n)}]|_{y=-1}e^{in\Omega_{TL}}[e^{i(n+1)\alpha x}+e^{i(n-1)\alpha x}], \tag{B 7}$$

which contain aperiodic terms in the expressions for u_1, i.e. $(\widehat{Au})$, and v_1, i.e. $(\widehat{Av})$ of the following forms:

$$\widehat{Au}=DU_0^{(1)}e^{i\Omega_{TL}}+DU_0^{(-1)}e^{-i\Omega_{TL}}, \quad \widehat{Av}=DV_0^{(1)}e^{i\Omega_{TL}}+DV_0^{(-1)}e^{-i\Omega_{TL}}. \tag{B 8a,b}$$

It can be shown using the continuity equation and equation (B 4) that $\widehat{Av}$ is always zero while $\widehat{Au}$ is not zero except for $\Omega_{TL}=0, \pi$. As equation (B 3) is homogeneous, the non-zero solutions are associated solely with the inhomogeneities in the boundary conditions and, thus, the non-zero $\widehat{Au}$ is responsible for the creation of the drift.

https://doi.org/10.1017/jfm.2017.426 Published online by Cambridge University Press

REFERENCES

ABTAHI, A. & FLORYAN, J. M. 2017 Natural convection in corrugated slots. *J. Fluid Mech.* **815**, 537–569.

ABTAHI, A., HOSSAIN, M. Z. & FLORYAN, J. M. 2016 Spectrally accurate algorithm for analysis of convection in corrugated conduits. *Comput. Maths Applics.* **72**, 2636–2659.

AHLERS, G., GROSSMANN, S. & LOHSE, D. 2009 Heat transfer and large scale dynamics in turbulent Rayleigh–Bénard convection. *Rev. Mod. Phys.* **81**, 503–537.

ASGARIAN, A., HOSSAIN, M. Z. & FLORYAN, J. M. 2016 Rayleigh–Bénard convection driven by a long wavelength heating. *J. Theor. Comput. Fluid Mech.* **30**, 313–337.

BELTRAME, P., KNOBLOCH, E., HÄNGGI, P. & THIELE, U. 2011 Rayleigh and depinning instabilities of forced liquid ridges on heterogeneous substrates. *Phys. Rev.* E **83**, 016305.

BÉNARD, H. 1900 Les tourbillons cellulaires dans une nappe liquide. *Revue Générale Science Pure et Applique* **11**, 1261–1271.

BODENSCHATZ, E., PESCH, W. & AHLERS, G. 2000 Recent developments in Rayleigh–Bénard convection. *Annu. Rev. Fluid Mech.* **32**, 709–778.

BUSSE, F. H. & CLEVER, R. M. 1979 Instabilities of convection rolls in a fluid of moderate Prandtl number. *J. Fluid Mech.* **91**, 319–335.

CHANDRASEKHAR, S. 1961 *Hydrodynamic and Hydromagnetic Stability*. Oxford University Press.

CHILLA, F. & SCHUMACHER, J. 2012 New perspectives in turbulent Rayleigh–Bénard convection. *Eur. Phys. J.* E **35**, 58–82.

CLEVER, R. M. & BUSSE, F. H. 1974 Transition to time-dependent convection. *J. Fluid Mech.* **65**, 625–645.

FINNEY, M. A., COHEN, J. D., MCALLISTER, S. S. & JOLLY, W. M. 2012 On the need for a theory of wildland fire spread. *Intl J. Wildland Fire* **22**, 25–36.

FLORYAN, D. & FLORYAN, J. M. 2015 Drag reduction in heated channels. *J. Fluid Mech.* **765**, 353–395.

FREUND, G., PESCH, W. & ZIMMERMANN, W. 2011 Rayleigh–Bénard convection in the presence of spatial temperature modulations. *J. Fluid Mech.* **673**, 318–348.

GOLUSKIN, D. & DOERING, C. R. 2016 Bounds for convection between rough boundaries. *J. Fluid. Mech.* **804**, 370–386.

HASSANZADEH, P., CHINI, G. P. & DOERING, C. R. 2014 Wall to wall optimal transport. *J. Fluid Mech.* **751**, 627–662.

HOSSAIN, M. Z. & FLORYAN, J. M. 2013*a* Instabilities of natural convection in a periodically heated layer. *J. Fluid Mech.* **733**, 33–67.

HOSSAIN, M. Z. & FLORYAN, J. M. 2013*b* Heat transfer due to natural convection in a periodically heated slot. *ASME J. Heat Transfer* **135**, 022503.

HOSSAIN, M. Z. & FLORYAN, J. M. 2014 Natural convection in a fluid layer periodically heated from above. *Phys. Rev.* E **90**, 023015.

HOSSAIN, M. Z. & FLORYAN, J. M. 2015*a* Mixed convection in a periodically heated channel. *J. Fluid Mech.* **768**, 51–90.

HOSSAIN, M. Z. & FLORYAN, J. M. 2015*b* Natural convection in a horizontal fluid layer periodically heated from above and below. *Phys. Rev.* E **92**, 02301.

HOSSAIN, M. Z. & FLORYAN, J. M. 2016 Drag reduction in a thermally modulated channel. *J. Fluid Mech.* **791**, 122–153.

HOSSAIN, M. Z. & FLORYAN, J. M. 2017 Natural convection under sub-critical conditions in the presence of heating non-uniformities. *Intl J. Heat Mass Transfer* **114**, 8–19.

HOSSAIN, M. Z., FLORYAN, D. & FLORYAN, J. M. 2012 Drag reduction due to spatial thermal modulations. *J. Fluid Mech.* **713**, 398–419.

HUGHES, G. O. & GRIFFITHS, R. W. 2008 Horizontal convection. *Annu. Rev. Fluid Mech.* **40**, 185–208.

HUSAIN, S. Z. & FLORYAN, J. M. 2007 Immersed boundary conditions method for unsteady flow problems described by the Laplace operator. *Intl J. Numer. Meth. Fluids* **46**, 1765–1786.

HUSAIN, S. Z. & FLORYAN, J. M. 2010 Spectrally-accurate algorithm for moving boundary problems for the Navier–Stokes equations. *J. Comput. Phys.* **229**, 2287–2313.

https://doi.org/10.1017/jfm.2017.426 Published online by Cambridge University Press

KRISHNAN, M., UGAZ, V. M. & BURNS, M. A. 2002 PCR in a Rayleigh–Bénard convection cell. *Science* **298**, 793.

LENARDIC, A., MORESI, L., JELLINEK, A. M. & MANGA, M. 2005 Continental insulation, mantle cooling, and the surface area of oceans and continents. *Earth Planet. Sci. Lett.* **234**, 317–333.

LOHSE, D. & XIA, K.-Q. 2010 Small-scale properties of turbulent Rayleigh–Bénard convection. *Annu. Rev. Fluid Mech.* **42**, 335–364.

MARCQ, S. & WEISS, J. 2012 Influence of sea ice lead-width distribution on turbulent heat transfer between the ocean and the atmosphere. *Cryosphere* **6**, 143–156.

MAXWORTHY, T. 1997 Convection into domains with open boundaries. *Annu. Rev. Fluid Mech.* **29**, 327–371.

MCCOY, J. H., BRUNNER, W., PESCH, W. & BODENSCHATZ, E. 2008 Self-organization of topological defects due to applied constraints. *Phys. Rev. Lett.* **101**, 254102.

MOHAMMADI, A. & FLORYAN, J. M. 2012 Mechanism of drag generation by surface corrugation. *Phys. Fluids* **24**, 013602.

RAYLEIGH, J. W. S. 1916 On convection currents in a horizontal layer of fluid, when the higher temperature is on the under side. *Phil. Mag.* **32**, 529–546.

RIPESI, P., BIFERALE, L., SBRAGAGLIA, M. & WIRTH, A. 2014 Natural convection with mixed insulating and conducting boundary conditions: low- and high-Rayleigh-number regimes. *J. Fluid Mech.* **742**, 636–663.

RIZWAM, A. M., DENNIS, L. Y. C. & LIU, C. 2008 A review on the generation, determination and mitigation of urban heat island. *J. Environ. Sci.* **20**, 120–128.

SEIDEN, G., WEISS, S., MCCOY, J. H., PESCH, W. & BODENSCHATZ, E. 2008 Pattern forming system in the presence of different symmetry-breaking mechanisms. *Phys. Rev. Lett.* **101**, 214503.

SIGGERS, J. H., KERSWELL, R. R. & BALMFORTH, N. J. 2004 Bounds on horizontal convection. *J. Fluid Mech.* **517**, 55–70.

TOPPALADODDI, S., SUCCI, S. & WETTLAUFER, J. S. 2015 Tailoring boundary geometry to optimize heat transport in turbulent convection. *Eur. Phys. Lett.* A **111**, 44005.

WEISS, S., SEIDEN, G. & BODENSCHATZ, E. 2012 Pattern formation in spatially forced thermal convection. *New J. Phys.* **14**, 053010.

WINTERS, K. B. & YOUNG, W. R. 2009 Available potential energy and buoyancy variance in horizontal convection. *J. Fluid Mech.* **629**, 221–230.

https://doi.org/10.1017/jfm.2017.426 Published online by Cambridge University Press